Chen *et al. Journal of Nanobiotechnology* (2025) 23:114
https://doi.org/10.1186/s12951-025-03176-6

Journal of Nanobiotechnology

RESEARCH **Open Access**

RGD hydrogel-loaded ADSC extracellular vesicles mitigate uranium-induced renal injury *via* TLR4/NF-κB pathway inhibition

Xi Chen[1,2†], Chun-Mei Dai[2,3†], Bin Zhang[2,3], Wan-Xin Zhang[2,3], Zheng-Hong Huang[2,4], Jiu-Yi Jiang[2,3], Shi-Qi Hu[1], Jia-Hua Ma[1*] and Jia-Fu Feng[1,2*]

Abstract

Background Uranium-induced kidney damage represents a major health concern due to its toxic effects, including mitochondrial dysfunction and inflammation. Mitochondrial DNA (mtDNA)-mediated pyroptosis is a critical pathway in the pathogenesis of renal injury. The toll-like receptor 4 / nuclear factor-kappa B (TLR4/NF-κB) signaling pathway plays a pivotal role in this process. Recent studies have shown that extracellular vesicles derived from adipose-derived stem cells (ADSCs-EVs) possess therapeutic potential due to their anti-inflammatory and regenerative properties. Incorporating ADSCs-EVs into arginine-glycine-aspartate (RGD), hydrogels may enhance their stability and therapeutic efficacy in vivo. This study aims explore the molecular mechanism by which RGD hydrogel-loaded ADSCs-EVs modulate mtDNA-mediated pyroptosis by suppressing the TLR4/NF-κB signaling pathway to alleviate uranium-induced kidney injury.

Results Repairing mitochondrial dysfunction was found to mitigate mtDNA leakage, thereby inhibiting renal pyroptosis. ADSCs-EVs alleviated uranium-induced renal cell damage by suppressing the TLR4/NF-κB signaling pathway. In vivo animal experiments confirmed that RGD hydrogel-loaded ADSCs-EVs enhanced their stability in the body and improved their therapeutic efficacy against kidney injury.

Conclusion Our findings reveal that RGD hydrogel-loaded ADSCs-EVs effectively inhibit the TLR4/NF-κB signaling pathway, preventing mtDNA-mediated pyroptosis and alleviating uranium-induced kidney damage. This elucidation provides a novel strategy for utilizing RGD hydrogel-loaded ADSCs-EVs in treating kidney injury.

[†] Xi Chen and Chun-Mei Dai contributed equally to this work and should be considered the first authors.

*Correspondence:
Jia-Hua Ma
jiahuama@swust.edu.cn
Jia-Fu Feng
jiafufeng@sc-mch.cn

Full list of author information is available at the end of the article

Graphical abstract

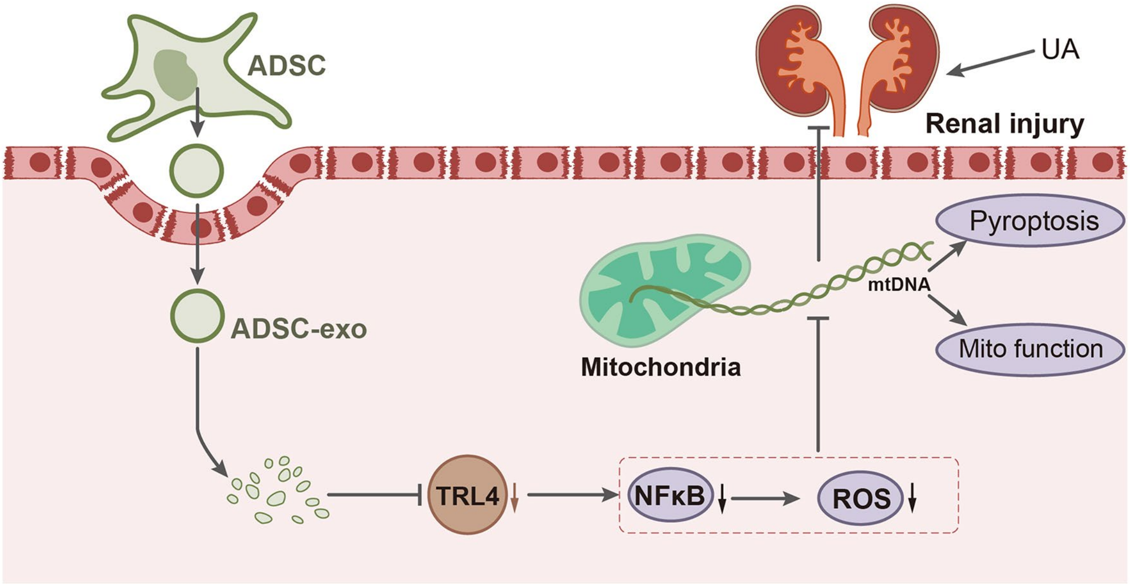

Keywords RGD hydrogel, ADSCs-EVs extracellular vesicles, TLR4/NF-κB signaling pathway, Mitochondrial DNA, Pyroptosis, Kidney injury

Introduction

In recent years, there has been a growing concern over uranium-induced kidney damage [1]. Uranium, as a heavy metal widely present in the environment, poses potential toxicity that could pose serious threats to both human health and the environment [2]. The use of uranium has been increasing, particularly in nuclear energy development and military activities, thereby exacerbating the issue of uranium-induced kidney damage. Currently, there is a lack of effective treatment strategies to mitigate uranium-induced kidney damage, necessitating urgent research efforts to safeguard human health and the environment [3, 4].

Recent studies indicate that pyroptosis is a significant mechanism underlying uranium-induced kidney damage [5]. Mitochondria are critical organelles in cells, and their dysfunction can lead to cell death [6–8]. During mitochondrial damage, the release of mtDNA plays a key role in pyroptosis. The release of mtDNA may exacerbate inflammatory responses, thereby worsening the extent of kidney damage [9–11]. Additionally, previous studies have demonstrated that mtDNA can activate toll-like receptor 4 (TLR4), triggering inflammatory responses during acute injuries [12, 13]. Therefore, further research on mtDNA-mediated pyroptosis is crucial for understanding and treating uranium-induced kidney damage [6, 14, 15].

Extracellular vesicles (EVs) play a significant role in regulating mitochondrial dysfunction, thereby helping to reduce inflammatory responses. This regulatory role likely involves influencing mitochondrial dynamics and function within cells, ultimately impacting DNA-associated pyroptosis. EVs can mediate intercellular signaling by transferring biomolecules such as miRNAs and proteins, influencing both physiological and pathological processes. The applications of EVs in regenerative medicine, anti-inflammatory therapies, and cancer treatment are gaining widespread attention [16]. ADSCs-EVs are cell-derived nanosized vesicles released by ADSCs [17]. These EVs are crucial in cell communication and regenerative therapy [18–20]. Previous studies have shown that ADSCs-EVs exhibit potential therapeutic effects on renal injuries, such as ischemia-reperfusion kidney injury [21] and lipopolysaccharide (LPS)-induced acute kidney injury [22]. However, there are no reports on the effects of ADSCs-EVs on uranium-induced renal injury. Therefore, investigating the role of ADSCs-EVs in alleviating uranium-induced renal damage and its molecular mechanisms is of significant clinical importance for developing novel treatment strategies targeting uranium-induced kidney injury.

This study aims to explore the role of ADSCs-EVs in ameliorating uranium-induced renal damage and its molecular mechanisms by modulating mtDNA-mediated pyroptosis through the inhibition of the TLR4/NF-κB signaling pathway. The findings of this study will provide a basis and new insights for developing and designing innovative treatment strategies for uranium-induced kidney injury. This research is of crucial clinical significance in searching for effective methods to address uranium-induced renal damage issues. The contribution of this study lies in offering new research directions and treatment strategies, providing a breakthrough in the treatment of uranium-induced kidney injury, and potentially guiding and aiding researchers and clinicians seeking to tackle this serious threat. By enhancing the understanding of the application of ADSCs-EVs in kidney injury treatment, this research holds promise in offering new possibilities for the treatment of uranium-induced renal damage and contributing to the protection of human health and the environment.

Materials and methods

Bioinformatics analysis

Information related to the TLR4 gene was obtained from the Genecards database (www.genecards.org). Protein interaction data for TLR4 were obtained from the STRING database (https://string-db.org/) and visualized using Cytoscape 3.8.2 software. The ranking of nodes in the protein-protein interaction (PPI) network was performed based on methods described in the literature [23]. To better understand the biological functions of these genes, gene ontology (GO) and Kyoto Encyclopedia of Genes and Genomes (KEGG) enrichment analyses were carried out using the "ClusterProfiler" package in R software. GO functional enrichment analysis was conducted at three levels: biological processes (BP), cellular components (CC), and molecular functions (MF), with a significance threshold of $P < 0.05$ [24].

Construction of a kidney injury cell model

The toxic effects of UA, with the molecular formula: $UO_2(AC)_2 \cdot 2H_2O$, molecular weight: 426.16228, and 99% purity (Shanghai JiZhi Biochemical Technology Co., Ltd., Shanghai, China) were studied in human proximal tubule epithelial cells (HK-2, B164615, obtained from Ningbo Mingzhou Biotechnology Co., Ltd.) to establish a model of uranium-induced kidney injury [25]. HK-2 cells were cultured in DMEM medium containing 10% fetal bovine serum and maintained in optimal conditions at 37 °C with a CO_2 concentration of 5%. Unless otherwise specified, all cell culture reagents were purchased from Thermo Fisher, Gibco. The UA group was treated with various concentrations (0.1, 0.5, 1.0, 5.0, 10.0, 20.0, 50.0, 100.0, 200.0 μmol/L) of uranyl solution (diluted from a 200.0 μmol/L stock solution) for 24 h; the Control group was treated with an equivalent volume of saline solution. Furthermore, the UA group was further divided into the following subgroups: Mdivi-1 (MedChemExpress) group, treated with 10 μmol of the mitochondrial fission inhibitor Mdivi-1; DMSO group, treated with an equivalent volume of DMSO (China National Pharmaceutical Group) instead of Mdivi-1; ADSCs-EVs group, treated with 100 μg/mL of ADSCs-EVs for 24 h; PBS group, treated with an equivalent volume of PBS instead of ADSCs-EVs; ADSCs-EVs + PMA group, treated with 100 μg/mL of ADSCs-EVs and 20 ng/mL of the NF-κB activator PMA (phorbol-12-myristate-13-acetate, MedChemExpress) for 24 h; ADSCs-EVs + DMSO group, treated with an equivalent volume of DMSO instead of PMA [26]. At a uranium concentration of 50.0 μmol/L, the cell viability of HK-2 cells was close to 50%. Therefore, the final selected concentration for cell treatment in establishing the uranium-induced kidney injury cell model was 50.0 μmol/L. After 24 h of treatment, morphological changes in UA-treated HK-2 cells, such as vacuole formation and abnormal mitochondrial morphology, were observed under a microscope [25].

Detection of cytoplasmic mtDNA in kidney cells using qPCR

HK-2 cells were lysed using Triton X-100 lysis buffer (Sigma-Aldrich) to separate nuclear and cytoplasmic fractions [27]. Cells were collected in 1.5 mL centrifuge tubes, washed twice with PBS, and the excess PBS was removed. A buffer containing 0.5% Triton X-100 (pH 7.4) was added to the cells, which were gently suspended and then centrifuged at 12,000 g for 10 min at 4 °C to collect the supernatant. The nuclear pellet was resuspended and incubated at 65 °C for 30 min in a water bath until completely lysed. Following a second centrifugation at 12,000 g for 10 min at 4 °C, the nuclear fraction (supernatant) was collected.

Genomic DNA was extracted from both the nuclei and cytoplasmic fractions (Qiagen) using Qiagen DNA purification kits, and concentrations and purities were determined. Then, qPCR was performed to detect the mtDNA copy numbers in the fractions. Specific primers were designed and synthesized for two mtDNA gene segments, MT-ND1 and MT-ND2, based on previous literature [28] (Table S1). The qPCR reactions were conducted to quantify the mtDNA copy numbers in the nuclear and cytoplasmic fractions.

Cellular and renal mitochondrial morphology

Mitochondria in cells were labeled with MitoTracker Deep Red (100 nmol/L, Sigma-Aldrich) and incubated at 37 °C for 30 min. Observations were conducted using confocal microscopy (Leica TCS SP5, Wetzlar, Germany). Mitochondrial fluorescence was excited with a 633 nm laser and recorded at 558–617 nm. The length of the mitochondria was quantified and calculated using Image J software. Renal tissue samples were fixed and imaged with an H-7500 transmission electron microscope (Hitachi, Japan), and the mitochondrial length and cristae density of renal tissues were assessed using Image J software [14].

Detection of mitochondrial membrane potential (MMP)

Cell samples were washed with culture medium and re-suspended on coverslips for further processing. JC-1 dye (Invitrogen) was applied according to the manufacturer's instructions. Observation were performed under a fluorescence microscope, with an excitation wavelength of 488 nm and an emission wavelength of 590 nm. JC-1 forms aggregates that emit red fluorescence in cells with high MMP, whereas it remains monomeric and emits green fluorescence in cells with low MMP states [29].

Biochemical indicator detection

Urea levels were measured using the urease-glutamate dehydrogenase method, while creatinine levels were determined using the creatinine oxidase method, both performed on the LABOSPECT 008α fully automated biochemical analyzer (Hitachi, Japan). Commercial reagent kits were obtained from Sichuan Maccura Biotechnology Co., Ltd. (Maccura, China) [30].

Detection of reactive oxygen species (ROS) levels in renal cells

HK-2 renal cells treated with uranium and control cells were collected, washed, and suspended in PBS. The cells were then incubated with 10 μM DCFH-DA (2',7'-dichlorofluorescein diacetate, Sigma-Aldrich, Darmstadt, Germany) in phenol red-free culture medium for 30 min at 37 °C in a 5% CO_2 atmosphere. DCFH-DA enters cells, where it is hydrolyzed by cellular esterases to convert into DCFH. In the presence of ROS, DCFH is oxidized to the fluorescent compound DCF. Following incubation, the cells were washed three times with PBS to remove unabsorbed DCFH-DA. Detection was performed using a fluorescence microplate reader (Flx800, Biotek, USA) with an excitation wavelength of 488 nm and an emission wavelength of 525 nm. The ROS levels of each sample were expressed as relative fluorescence intensity, calculated as Increase in Fluorescence (%) = (F30 - F0) / F30 × 100%, where F30 and F0 represent the fluorescence intensity at 30 min and 0 min of incubation, respectively. Finally, the obtained data were statistically analyzed to compare the difference in ROS levels between the treatment group and the control group of renal cells [14].

Enzyme-linked immunosorbent assay (ELISA)

The supernatant of HK-2 cells from each group was centrifuged at 1500×g for 15 min. The LDH levels were measured using an ELISA assay kit (P07195) from R&D Systems Inc. The specific operational steps were followed as: first, the corresponding number of reaction wells for the samples were prepared and all reagents were thoroughly mixed. Second, 50 μL of diluted standards and test samples were added to each well. Third, the wells were incubated at 37 °C for 30 min, then the liquid was gently shaken off. Each well was filled with wash solution, gently shaken for 30 s, then the wash solution was shaken off. This process was repeated three times. Fourth, 80 μL HRP was added to each well, gently shaken to mix, and incubated at 37 °C for 30 min. Fifth, step three was repeated. Sixth, 50 μL of substrates A and B were added to each well, mixed gently, and incubated at 37 °C for 10 min. Seventh, the plate was removed from the incubator and 50 μL of stop solution was quickly added to each well. Eighth, the OD values of each well at a wavelength of 450 nm were measured using the Bio-Tek Epoch microplate spectrophotometer. Three replicate wells were set up for each sample [31, 32].

Preparation of uranyl acetate (UA) solution

A sample of 220.8 mg of UA dihydrate (molecular formula: $UO_2(AC)_2 \cdot 2H_2O$, molecular weight: 426.16228, 99.0% purity; Shanghai Jizhi Biochemical Technology Co., Ltd., Shanghai, China) was dissolved in 100.0 ml of physiological saline solution. The solution was then filtered through a 0.22 μm sterile syringe filter (NovoBiotec, Beijing, China) to obtain a 2.0 mg/ml UA solution. The uranium concentration in this solution was confirmed using a NexION 300Q Inductively Coupled Plasma Mass Spectrometer (PerkinElmer, Shelton, USA).

Construction of a rat model of kidney Injury

Eight-week-old Sprague-Dawley (SD) rats were obtained from Beijing Vital River Laboratory Animal Technology Co., Ltd. (Beijing, China). The rats were housed under pathogen-free conditions at 26–28 °C with 50–65% humidity and a 24-hour light-dark cycle. All animal experiments complied with ethical standards and were approved by the Animal Ethics Committee of the institution (No. 22-07-127).

To induce kidney injury, each rat in the UA group received a single intraperitoneal injection of 0.2 mL of a working solution containing 1.0 μmol U to induce acute uranium nephrotoxicity. Rats in the Sham group were injected intraperitoneally with an equivalent volume of saline. Four days post-injection, the rats were euthanized using CO_2, and urine, blood, and kidney tissue samples were collected for subsequent experiments [33].

Hematoxylin and eosin staining

Rat kidney tissue slices were deparaffinized and hydrated following the instructions provided with the Hematoxylin and Eosin (H&E) staining kit instructions (PT001, Shanghai Bogu Bio-Technology Co., Ltd., Shanghai, China). The procedure included staining with hematoxylin at room temperature for 10 min, rinsing in running water for 30 to 60 s, differentiation in 1% hydrochloric acid alcohol for 30 s, immersion in running water for 5 min. Eosin staining was performed at room temperature for 1 min, followed by dehydration through a graded alcohol series (70%, 80%, 90%, 95%, 100%, each for 1 min) and clearing with xylene (1 min for each of two xylene solutions). The tissue sections were mounted using the neutral mounting medium in a fume hood and observed for morphological changes in kidney tissues using an optical microscope (BX50; Olympus Corp, Tokyo, Japan) for image capture and analysis [31, 34].

Isolation and identification of adipose-derived mesenchymal stem cells

Adipose tissue samples, obtained from individuals undergoing health screening, were aseptically minced into 0.5 mm fragments and digested with 0.2% collagenase I. The cells were cultured in low-glucose DMEM supplemented with 10% fetal bovine serum and 1% penicillin-streptomycin. Their morphological characteristics were observed, and cell surface markers (CD29, CD44, CD31, and HLA-DR) were analyzed using flow cytometry [35, 36].

Isolation and identification of EVs

Prior to collecting the conditioned medium of adipose-derived mesenchymal stem cells (ADSCs), it is recommended to replace the serum-containing culture medium with a chemically defined, xeno- and blood-free serum substitute, Oxium™ EVs (Regeneron Pharmaceuticals, USA) [37] and incubate it for 24–48 h to eliminate extracellular vesicle contamination from the serum. Subsequently, filter the medium through a 0.22 μm filter to remove cells and cell debris. Although this step may result in the filtration of some EVs, it facilitates the subsequent centrifugation steps while eliminating large cells and cell debris, thereby reducing interference during centrifugation. Next, centrifuge at 300 × g for 10 min at a low speed to remove cell residues and large particles. Following this, centrifuge at 2000 × g for 20 min at a medium speed to eliminate apoptotic bodies and large microvesicles. Centrifuge at 10,000 × g for 30 min at a high speed to remove small microvesicles. Finally, centrifuge at 100,000 × g for 60–90 min at an ultra-high speed to pellet the EVs. Discard the supernatant, resuspend the pellet in PBS or serum-free medium, and wash the EVs again at 100,000 × g in ultra-high-speed centrifugation. Discard the supernatant and resuspend the pellet in PBS or serum-free medium to obtain the extracellular vesicle sample. Various methods can identify EVs, including transmission electron microscopy (TEM), NTA, flow cytometry, and Western blot. TEM is used to observe the morphology and size of EVs, while NTA measures the size and concentration of EVs. Flow cytometry and Western blot are employed to detect specific protein markers of EVs, such as CD63 (1:200, PA5-92370, ThermoFisher), CD81 (1:200, MA5-32333, ThermoFisher), CD9 (1:200, MA5-31980, ThermoFisher), Cytochrome C (1:500, sc-13560, Santa Cruz), and Calnexin (1:200, sc-80645, Santa Cruz), to assess the presence, quantity, and integrity of EVs [38].

TEM

EV samples were isolated and fixed in 0.1 mol/L PBS containing 2% paraformaldehyde. A 5 μL sample was placed on a carbon-coated 400-mesh Cu/Rh grid (Ted Pella Inc., Redding, CA) and left at room temperature for 1 min. Excess liquid was removed with filter paper, and the sample was stained with 1% uranyl acetate (UA) (Polysciences, Inc., Warrington, PA) in three steps. The grids were examined using a JEOL TEM-2000 EX II electron microscope (MA-tek, Hsinchu, Taiwan) to assess the EVs' double lipid layer structure [38].

Nanoparticle tracking analysis (NTA)

The size and concentration of hADSC EVs were determined using the NanoSight NS300 system (Malvern Instruments, UK). All samples were diluted in PBS to a final volume of 1 ml. The following settings were applied according to the manufacturer's instructions: the camera was set to sCMOS mode with a camera level 16. For each measurement, the cell temperature was set to 25 °C, and the injection pump speed was maintained at 70 μL/s. Subsequent analysis was carried out using the NanoSight Software NTA 3.4 Build 3.4.003, with a threshold set at 5. Hardware parameters included an embedded laser with a power of 45 mW at a wavelength of 488 nm and a sCMOS camera. Within the NTA 3.4 software, size distribution plots, as well as the mean/mode size values and standard deviation, could be calculated [38].

Cell uptake of EVs experiment

ADSCs-EVs were labeled using the PKH26 labeling kit (Sigma-Aldrich, USA). The EVs were resuspended in 1 mL of Diluent C, and 4 μL of PKH26 ethanol dye solution was added to the Diluent C to prepare a 4×10^{-6} M dye solution. The 1 mL of ADSCs-EVs suspension was mixed with the dye solution for 5 min. The PKH26-labeled ADSCs-EVs were co-incubated with HK-2 cells at 37 °C for 12 h. The cells were fixed with 4% PFA, washed with PBS, stained with 4', 6-diamidino-2-phenylindole (Sigma, D9542, USA) for nuclei, and the uptake of ADSCs-EVs by HK-2 cells was observed [39].

To determine the optimal concentration of ADSCs-EVs for treatment, different concentrations of EVs (25, 50, 100, 200 μg/mL) were labeled using PKH26 and co-incubated with HK-2 cells for 6 h. The fluorescence distribution of PKH26 was then detected using immunofluorescence to assess the uptake efficiency of ADSCs-EVs by the cells.

Western blot analysis

Tissue was lysed using RIPA lysis buffer containing PMSF (P0013B, Beyotime, China) to extract total protein. Cellular nuclear and cytoplasmic proteins were extracted using the Cell Nuclear and Cytoplasmic Protein Extraction Kit (P0028, Beyotime, China) following the manufacturer's instructions. The supernatant was used for determining the total protein concentration of each sample using the BCA assay kit (P0011, Beyotime, China), adjusted to 1 μg/μL. Subsequently, 100 μL of each sample supernatant was mixed with 1× SDS buffer containing β-mercaptoethanol, boiled at 100 °C for 10 min for denaturation, and stored at -80 °C.

An 8–12% SDS gel was prepared according to the target protein band size, and protein samples were loaded into individual lanes for electrophoresis. The proteins were transferred from the gel to a PVDF membrane (1620177, BIO-RAD, USA). The membrane was blocked in 5% non-fat milk at room temperature for 1–2 h, followed by overnight incubation at 4 °C with primary antibodies: TWNK (sc-293368, 1:200, Santa Cruz, CA), TFAM (ab131607, abcam, UK), PGC-1α (ab313559, abcam, UK), NRF1 (ab175932, 1:200, abcam, UK), NRF2 (ab62352, 1:200, abcam, UK), IL-1β (12703, 1:1000, Cell Signaling Technology, USA), IL-6 (ab9324, 1:1000, Abcam, Cambridge, UK), TNF-α (ab307164, 1:1000, Abcam, Cambridge, UK), GSDME (ab223877, 1:1000, Abcam, Cambridge, UK), GSDME-N (ab215191, 1:2000, Abcam, Cambridge, UK), GSDME-C (ab221843, 1:1500, Abcam, Cambridge, UK), Caspase (ab32351, 1:1000, Abcam, Cambridge, UK), Cleaved-Caspase-3 (ab32042, 1:1000, Abcam, Cambridge, UK), TLR4 (48-2300, 1:500, ThermoFisher, USA), p-p65 (ab76302, 1:1000, Abcam, Cambridge, UK), with GAPDH (ab8245, 1:1000, Abcam, Cambridge, UK) and PARP (ab191217, 1:1000, Abcam, Cambridge, UK) as internal controls.

After overnight incubation at 4 °C, the membrane was washed with TBST three times for 10 min each, incubated with an HRP-conjugated secondary antibody (goat anti-rabbit IgG H&L (HRP), ab97051, 1:2000, Abcam, Cambridge, UK) for 1 h, washed with TBST, and placed on a clean glass plate. ECL chemiluminescence detection reagents (abs920, Elabscience Biotechnology, Shanghai, China) A and B were mixed in the darkroom, added to the membrane, and then photographed using the Bio-Rad imaging system (BIO-RAD, USA). Analysis was performed using Quantity One v4.6.2 software, with the grayscale value of the corresponding protein band normalized to the internal control protein band representing relative protein levels. The experiment was repeated three times, and the average was calculated [14].

Detection of gene expression in cells or tissues using RT-qPCR

Total RNA was extracted from cell line samples using TRIzol reagent (15596-018, Solarbio, USA) and reverse transcribed into cDNA for measuring mRNA expression. The PrimeScript™ RT-PCR kit (TaKaRa, Mountain View, California, USA) was utilized for reverse transcription of total RNA. Primers designed and synthesized by Shanghai Generon Ltd. (Table S2) were employed for real-time quantitative PCR (RT-qPCR) reactions, with SYBR Premix Ex TaqTM (TaKaRa) used on the LightCycler 480 system (Roche Diagnostics, Pleasanton, California, USA) with β-actin as the reference gene. The relative transcription levels of the target gene were calculated using the comparative ΔΔCT method ($2^{-\Delta\Delta CT}$ method), where $\Delta\Delta CT = \Delta Ct$ experimental group - ΔCt control group. Here, ΔCt represents the difference between the cycle threshold (Ct) of the target gene and the reference gene. Ct signifies the cycle number at which the real-time fluorescence signal reaches a predetermined threshold, indicating exponential amplification [40–42]. Each sample was run in triplicate technical replicates, with three independent experiments conducted.

Immunofluorescence

Sterilized round glass slides were placed in a 24-well plate, and a single-cell suspension was prepared by trypsin digestion. After cell counting, 3×10^4 cells were seeded onto the slides and cultured at 37 °C with 5% CO_2. Once adhered, cells were washed with PBS, and 1 mL of 4% paraformaldehyde was added to each well for 15 min for fixation. Wells were then washed with PBS three times (5 min each).

Next, cells were permeabilized with 0.5% Triton X-100 for 15 min, followed by three PBS washes (5 min each). After removing PBS, 5% BSA blocking solution was added and incubated at room temperature for 1 h. The blocking solution was aspirated, and primary antibody p65 (Abcam, UK, ab32536, 1:100) was applied to the slides and incubated overnight at 4 °C.

The following day, slides were washed three times with PBS (5 min each), and Alexa Fluor 594 secondary antibody (Abcam, UK, ab150080, 1:100) was applied under light-protected conditions and incubated for 1 h at room temperature. After three additional PBS washes, DAPI solution was added and incubated for 15 min under light-protected conditions, followed by three PBS washes (5 min each).

In a dark room, slides were mounted using anti-fade medium. The round glass slides were carefully placed cell-side down onto the mounting medium. Samples were observed under a fluorescence microscope and stored at 4 °C in the dark [43].

Preparation and renal infusion of ADSCs-EVs/arginine-glycine-aspartate (RGD) hydrogel

Biotin-GFFYGRGD (3 mg, purchased from Beyotime) and sodium carbonate (adjusted to pH 7.4) were dissolved in 1.0 mL of PBS (pH 7.4) and subjected to a heating-cooling process. ADSCs-EVs at concentrations of 1.5, 3, 4.5, or 6 mg/mL were then added to the RGD-biotin hydrogel at different mass ratios (0.5:1, 1:1, 1.5:1, 2:1). The resulting hydrogel was incubated at 37 °C for 10 min to form the ADSCs-EVs/RGD hydrogel. Rheological testing was performed to assess the mechanical properties of the RGD hydrogel before and after loading ADSCs-EVs. Cy5 was used to label the RGD hydrogel for tracking its retention time in the kidney, while Gluc-lactadherin was used to label ADSCs-EVs to evaluate the impact of RGD hydrogel loading on the in vivo stability of ADSCs-EVs [39].

Renal Infusion of Hydrogel: The skin and peritoneum near the kidney were incised to expose the kidney. The incision size was kept just sufficient to expose the kidney to minimize wound size. The hydrogel was loaded into a pre-sterilized syringe or delivery device and slowly injected into the kidney. Care was taken to avoid excessive pressure during the procedure to prevent renal tissue damage or unintended leakage of the hydrogel. After ensuring no bleeding, the kidney was gently repositioned, and debridement and suturing were performed [44].

Kidney injury model grouping

The rat model of kidney injury was divided into four groups using the intrarenal injection method, with each group containing 10 rats. The groups were as follows: UA + ADSCs-EVs/RGD group, in which 40 μL of ADSCs-EVs/RGD was internally injected, containing 100 μg of ADSCs-EVs; UA + ADSCs-EVs/RGD + PMA group, where on the basis of the UA + ADSCs-EVs/RGD group, 1 mg/kg of NF-κB signaling pathway activator PMA was injected; UA + ADSCs-EVs group, with intrarenal injection of 100 μg of ADSCs-EVs; and UA + PBS group, receiving an equivalent volume of PBS instead of ADSCs-EVs. After 4 days, the rats were euthanized with CO_2, and urine, blood, and renal tissues were collected for subsequent experiments [39].

Statistical analysis

Statistical data analysis was conducted using R software version 4.1.1 (R Foundation for Statistical Computing, Vienna, Austria) and SPSS 21.0 software (IBM Corp., USA). Numerical data was presented in the form of mean ± standard deviation. To compare differences between different groups, independent samples t-tests were employed. For comparisons involving multiple groups, one-way analysis of variance (ANOVA) was utilized, followed by post hoc testing using Tukey's method for multiple comparisons. To assess the relationship between two variables, Pearson's correlation coefficient or Spearman's rank correlation coefficient was utilized for correlation analysis. Furthermore, to explore the interaction effects of different variables across different groups, consideration was given to interaction effects analysis within the framework of ANOVA. Additionally, appropriate non-parametric methods were applied for statistical analysis. For instance, in the case of non-normally distributed data or studies with small sample sizes, the Wilcoxon rank-sum test was employed for between-group comparisons. Comparisons of non-parametric data across multiple groups were performed using the Kruskal-Wallis test, followed by post hoc analysis using Dunn's multiple comparisons. Statistical significance was considered when the *P*-value was less than 0.05.

Results

Uranium-induced kidney injury manifests as mitochondrial damage and mtDNA leakage

To investigate the mechanisms of uranium-induced kidney injury, we treated HK-2 cells with UA to establish a model of heavy metal-induced renal cell damage. We measured the levels of lactate dehydrogenase (LDH) in the cell culture supernatant using ELISA. The results revealed a significant increase in LDH levels in the UA-treated group compared to the control group (Fig. 1A), indicating the successful construction of a model for renal cell injury.

Subsequently, we utilized Mitotracker staining to observe changes in mitochondrial morphology in renal cells. The results demonstrated that in the UA-treated group, there was severe fragmentation of mitochondria and a more dispersed internal structure compared to the control group (Fig. 1B). Total ROS levels in HK-2 cells were measured using DCFH-DA, showing a significant increase in ROS levels in the UA group compared to the control group (Fig. 1C). MMP was assessed using JC-1 staining, which revealed a significant decrease in MMP in the UA-treated cells compared to the control group, as evidenced by enhanced green fluorescence in the cells (Fig. 1D), indicating UA-induced mitochondrial damage.

Furthermore, we conducted qPCR to assess the cytoplasmic mtDNA copy number in renal cells after UA treatment, the experimental results displayed in Fig. 1E. In the UA-treated group, there was an increase in the abundance of ND1 and ND2 (mtDNA gene segments) in the cytosol, while the total DNA content within the cells did not increase, proving their significant leakage into the cytoplasm. These findings suggest that the renal

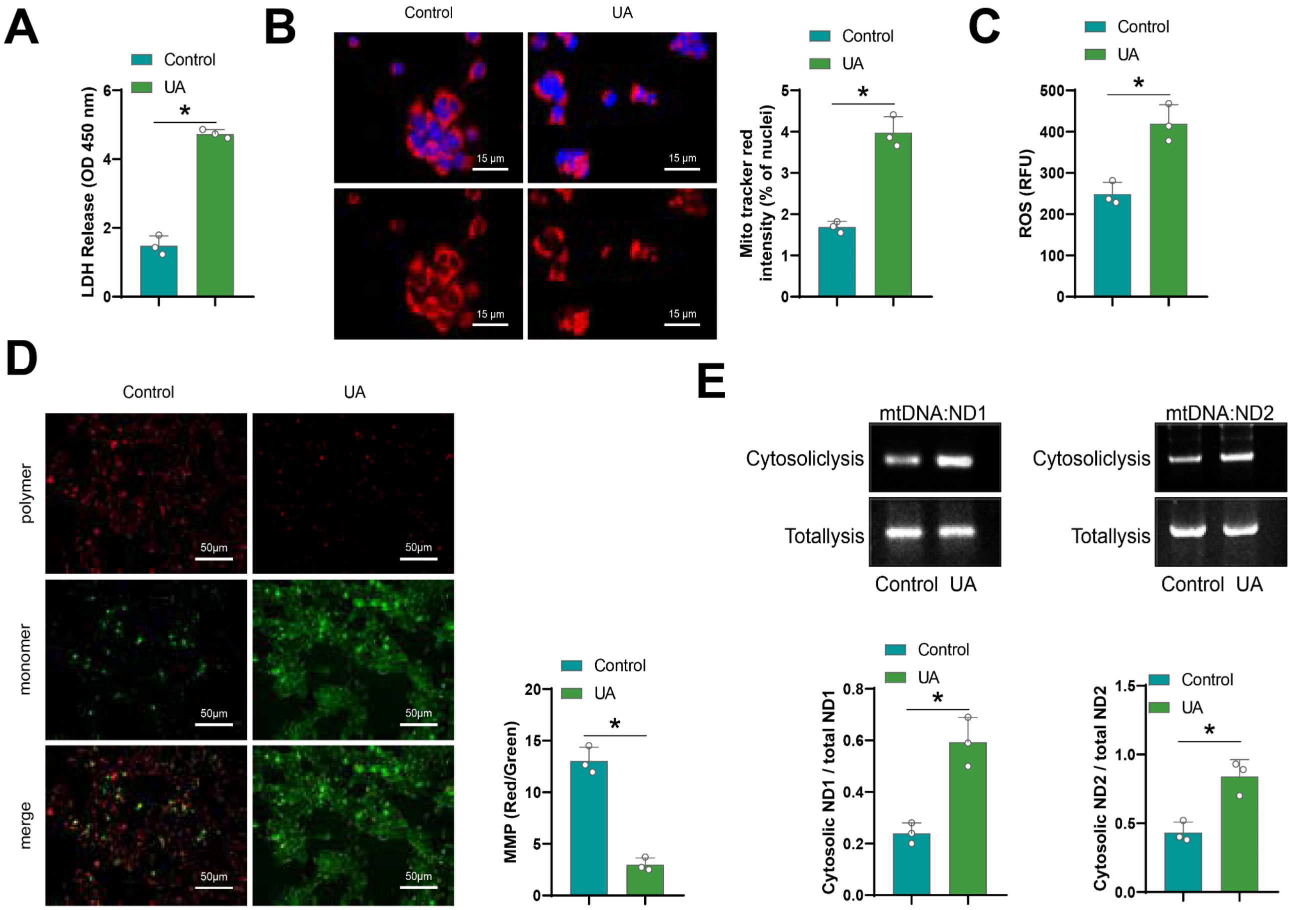

Fig. 1 Mitochondrial damage and mtDNA release in uranium-induced renal cell injury model. (**A**) LDH levels in the supernatant of HK-2 cells detected by ELISA; (**B**) Mitochondrial morphology in Control and UA groups stained with Mitotracker (red, mitochondria; blue, nucleus; scale bar = 15 μm); (**C**) Total ROS content in Control and UA group cells detected by DCFH-DA assay; (**D**) MMP in Control and UA groups detected by JC-1 staining, scale bar = 50 μm; (**E**) Cytoplasmic mtDNA copy number in renal cells after UA treatment detected by qPCR. All cellular experiments were repeated three times, * indicates $P < 0.05$

cell damage model induced by uranium can lead to mitochondrial damage and mtDNA leakage.

Subsequently, we utilized UA to establish a rat model of kidney injury. When compared to the Sham group, the rat kidneys in the UA group exhibited disorganized renal tissue morphology, lacking clear structures of glomeruli and renal tubules (Fig. 2A). Biochemical markers of kidney function (urea, creatinine) and oxidative stress indicators (malondialdehyde, glutathione, superoxide dismutase, and others) were significantly elevated in the UA group of rats (Fig. 2B), indicating the successful establishment of the rat model of kidney injury. Additionally, compared to the Sham group, the mRNA expression levels of mtDNA helicase (TWNK), mitochondrial transcription factor (TFAM), mitochondrial respiratory chain complex I (MRC I), mitochondrial respiratory chain complex IV (MRC IV), mitochondrial biogenesis-related factors PGC-1α, NRF1, NRF2, were significantly reduced in the UA group of rats (Fig. 2C). Western blot was used to detect protein levels of TWNK, TFAM, and mitochondrial biogenesis-related factors PGC-1α, NRF1, and NRF2. The results were consistent with those obtained *via* RT-qPCR (Fig. 2D). TEM images displayed in Fig. 2E revealed a substantial increase in mitochondrial fragmentation and vacuolization in the kidney tissues of UA rats compared to the Sham group. These findings further confirm in vivo that uranium-induced kidney injury leads to mitochondrial dysfunction.

Mitochondrial dysfunction repair reduces mtDNA leakage and suppresses renal pyroptosis

Previous studies have confirmed that mitochondrial dysfunction exacerbates the inflammatory process and promotes the release of inflammatory cytokines [45]. Renal pyroptosis is recognized as a primary manifestation of kidney injury [46]. Therefore, it is postulated that repairing mitochondrial dysfunction may be an effective approach to inhibit renal pyroptosis. Mdivi-1, a mitochondrial fission inhibitor, was used to treat UA group cells. Experimental findings indicated that the expression

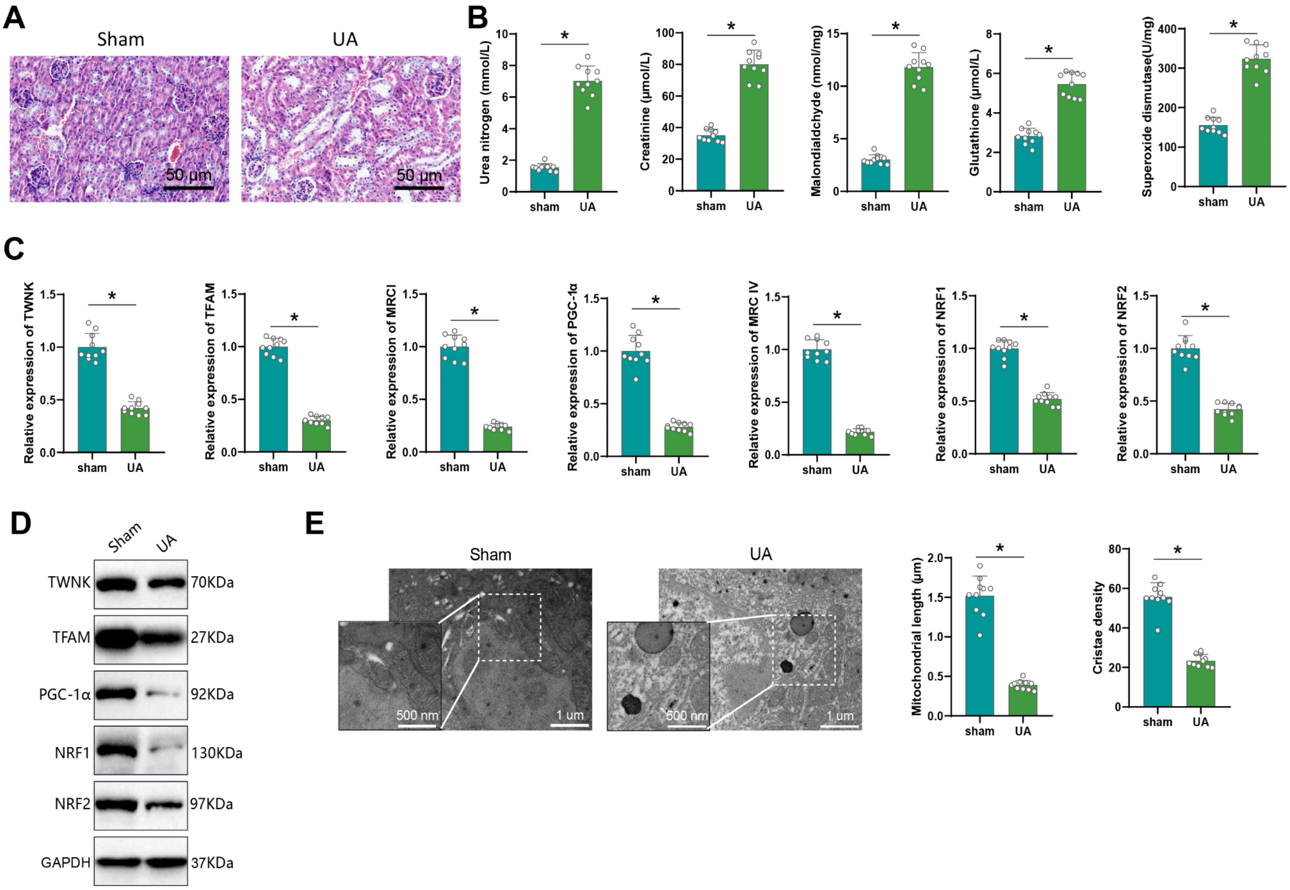

Fig. 2 Mitochondrial damage in uranium-induced kidney injury model. (**A**) Histological examination of rat kidney tissue morphology by H&E staining (scale bar = 50 μm); (**B**) Assessment of levels of urea, creatinine, malondialdehyde, glutathione, and superoxide dismutase in rat kidney tissue; (**C**) Measurement of mRNA levels of relevant cellular factors TWNK, TFAM, MRC I, MRC IV, PGC-1α, NRF1, and NRF2 in rat kidney tissue by RT-qPCR; (**D**) Protein levels of TWNK, TFAM, PGC-1α, NRF1, and NRF2 were detected via Western blot across different experimental groups; (**E**) TEM images displaying mitochondria in kidney tissues along with quantitative data on mitochondrial length and cristae density in each group. Scale bars = 1 μm / 500 nm. Each group consisted of 10 rats, * denotes $P < 0.05$

of IL-1β, IL-6, and TNF-α was significantly downregulated in the Mdivi-1-treated group (Fig. 3A). Moreover, mitochondrial fragmentation in the cells was reduced (Fig. 3B), ROS levels decreased significantly (Fig. 3C), and the MMP significantly increased, as evidenced by decreased green fluorescence in the cells (Fig. 3D). These results suggest that post-Mdivi-1 treatment effectively repaired mitochondrial damage in kidney cells. Additionally, following Mdivi-1 treatment, the abundance of mtDNA gene fragments ND1 and ND2 decreased in the cytosol, while the total DNA content in the cells remained unchanged (Fig. 3E), indicating that Mdivi-1 was beneficial in reducing mtDNA leakage. Furthermore, Western blot analysis of renal pyroptosis-related proteins revealed (Fig. 3F) a significant reduction in the expression of activated GSDME and Caspase-3 in cells treated with Mdivi-1. This indicates that Mdivi-1 treatment can suppress renal pyroptosis. In conclusion, repairing mitochondrial dysfunction contributes to the reduction of mtDNA leakage, thereby inhibiting renal pyroptosis.

ADSCs-EVs alleviate uranium-induced renal cell damage

EVs, as crucial mediators of intercellular communication, have been receiving increasing attention for their role in kidney injury. Studies have demonstrated that EVs can transmit critical signals in the pathological processes of the kidney, offering novel therapeutic targets [47]. Particularly, the application of ADSCs-EVs in the treatment of renal damage requires further investigation. In this study, we aim to explore the potential mechanisms and therapeutic effects of these EVs in kidney injury.

Initially, the efficacy of ADSCs isolation was verified using flow cytometry, with results indicating (Fig. S1A) that cells were highly positive for CD29 (92.28%) and CD44 (99.70%) while negative for CD31 (2.19%) and HLA-DR (2.55%). Moreover, staining with Oil-Red-O, Alizarin Red, and Alcian Blue revealed (Fig. S1B) the successful differentiation of ADSCs into adipocytes, osteoblasts, and chondrocytes, confirming the successful isolation of ADSCs. Subsequently, we isolated and extracted ADSCs-EVs. TEM and NTA demonstrated that

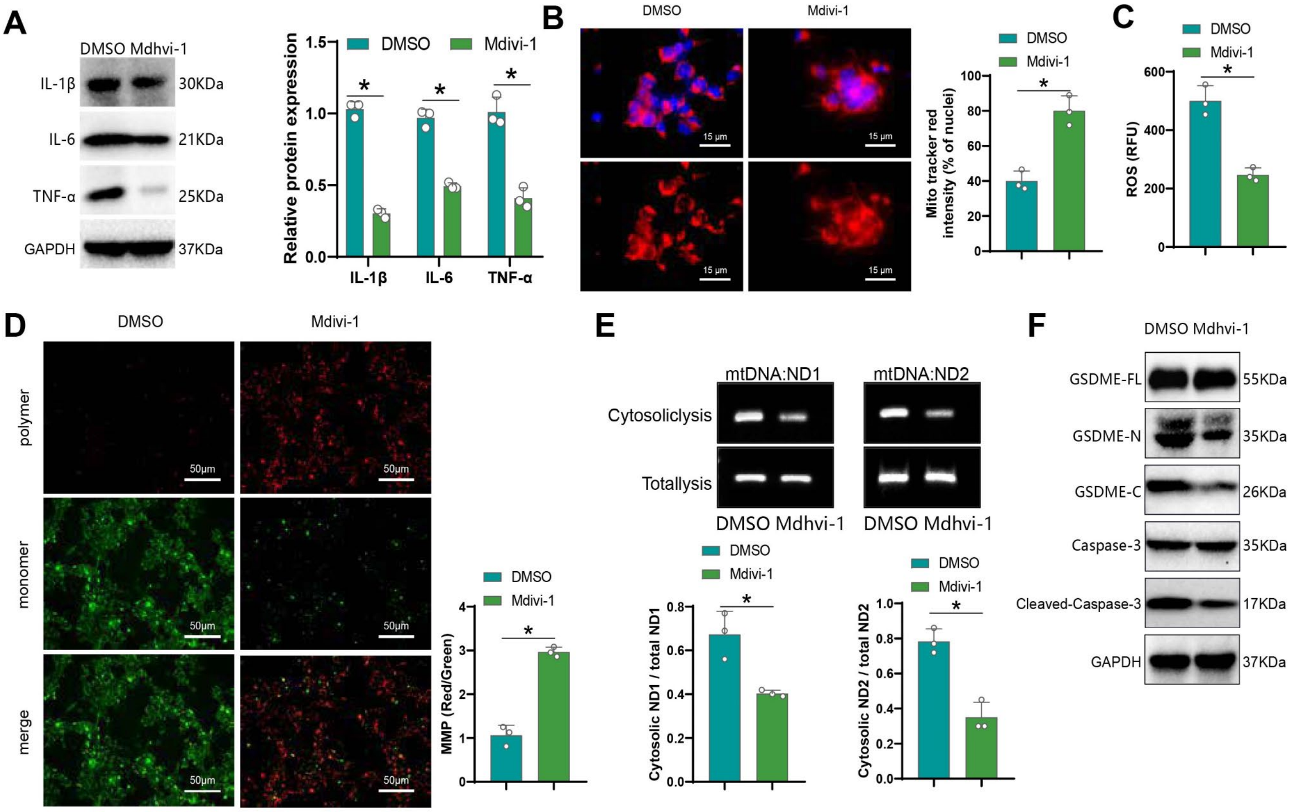

Fig. 3 The impact of restoring mitochondrial dysfunction on mtDNA leakage and renal cell pyroptosis. (**A**) Expression of IL-1β, IL-6, and TNF-α in each group of cells detected by Western blot; (**B**) Mitotracker staining to examine mitochondrial morphology in each group of cells (red for mitochondria, blue for cell nuclei; scale bar = 15 μm); (**C**) DCFH-DA reagent used to measure total ROS levels in each group of cells; (**D**) JC-1 staining to assess MMP in each group of cells, scale bar = 50 μm; (**E**) Quantitative PCR to determine cytoplasmic mtDNA copy numbers in each group of cells; (**F**) Expression of activated GSDME and Caspase-3 in each group of cells detected by Western blot. All cell experiments were performed in triplicate, with * indicating $P < 0.05$

the extracted particles exhibited typical circular or elliptical morphology (Fig. S1C), with particle sizes mainly ranging between 100 and 200 nm, consistent with EVs characteristics (Fig. S1D). Western blot analysis of EV surface markers revealed positivity for CD9, CD63, and CD81, while Cytochrome C and Calnexin were negative (Fig. S1E). These findings indicate the successful extraction of ADSCs-EVs, ensuring purity and integrity for further application in kidney injury research.

Initially, EVs at different concentrations (25, 50, 100, 200 μg/mL) were labeled with PKH26 and co-incubated with HK-2 cells for 6 h. The efficiency of EV uptake by the cells was evaluated using immunofluorescence. The results showed that the uptake of EVs by HK-2 cells was concentration-dependent, reaching saturation at an EV concentration of 100 μg/mL (Fig. S1F). Based on these findings, a concentration of 100 μg/mL was used for subsequent studies. Subsequent co-culturing of ADSCs-EVs with UA-induced renal cell injury model demonstrated a significant impact on renal cell function. The experimental findings revealed a significant downregulation of IL-1β, IL-6, and TNF-α expression in the ADSCs-EVs-treated group (Fig. 4A), accompanied by a reduction in mitochondrial fragmentation (Fig. 4B), a notable decrease in ROS levels (Fig. 4C), and a significant increase in MMP, as indicated by reduced green fluorescence in the cells (Fig. 4D). These observations suggest the beneficial effect of ADSCs-EVs in repairing mitochondrial damage in renal cells. Furthermore, post-treatment with ADSCs-EVs resulted in reduced abundance of ND1 and ND2 (mtDNA gene segments) in the cytosolic fraction, without any increase in total cellular DNA content (Fig. 4E), suggesting a role of ADSCs-EVs in mitigating mtDNA leakage. Additionally, Western blot analysis for renal pyroptosis-related proteins demonstrated a significant decrease in the expression of activated GSDME and Caspase-3 in cells treated with ADSCs-EVs (Fig. 4F), indicating the potential of these EVs in inhibiting renal pyroptosis. In conclusion, ADSCs-EVs can alleviate uranium-induced renal cell damage by repairing mitochondrial dysfunction, reducing mtDNA leakage, and suppressing pyroptosis.

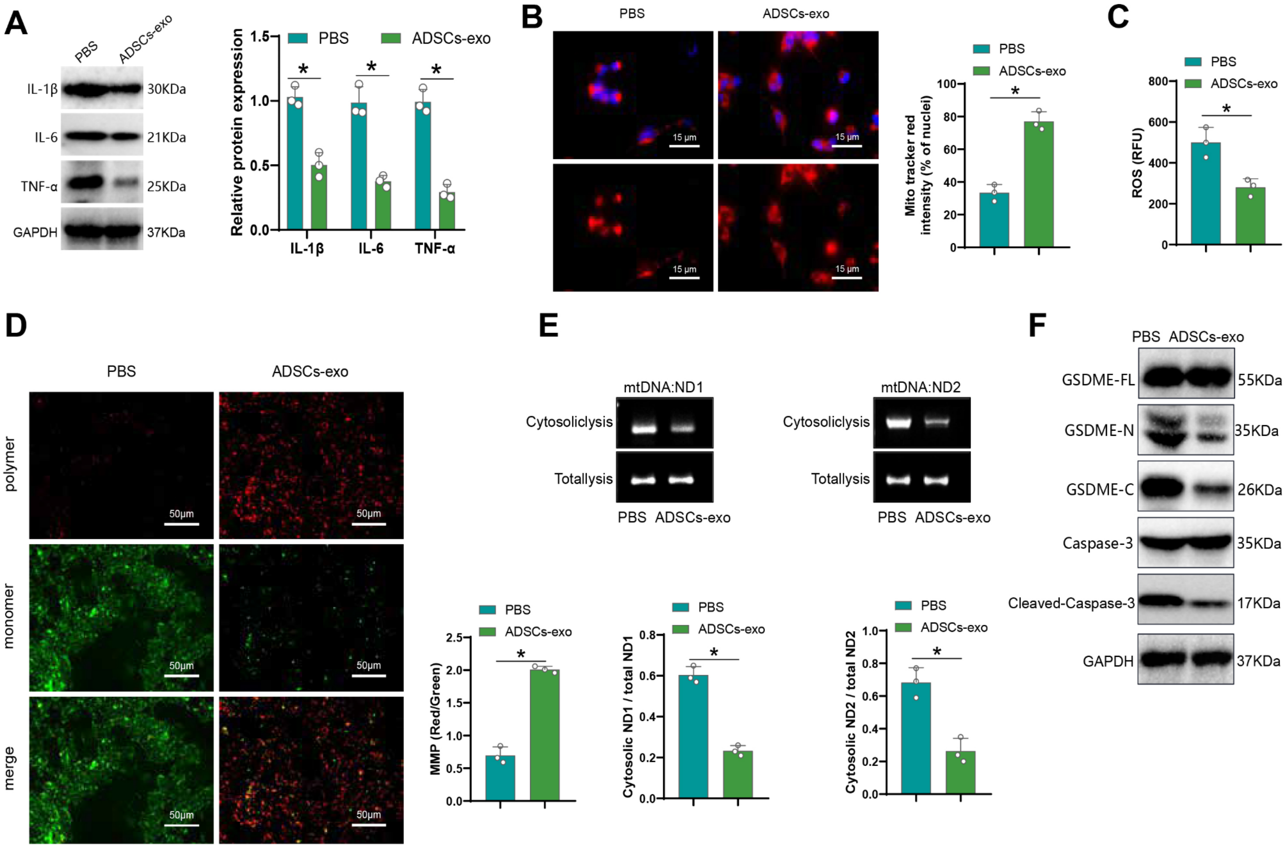

Fig. 4 ADSCs-EVs alleviate uranium-induced renal cell damage. (**A**) Western blot analysis was performed to assess the expression of IL-1β, IL-6, and TNF-α in each group of cells; (**B**) Mitotracker staining was used to examine the mitochondrial morphology of cells in each group (red, mitochondria; blue, nucleus; scale bar = 15 μm); (**C**) DCFH-DA reagent was employed to measure the total ROS levels in each group of cells; (**D**) JC-1 staining was conducted to evaluate the MMP of cells in each group, with a scale bar of 50 μm; (**E**) RT-qPCR was utilized to determine the cytoplasmic mtDNA copy number in each group of cells; (**F**) Western blot analysis was carried out to determine the expression of activated GSDME and Caspase-3 in each group of cells. All cell experiments were performed in triplicate, and * indicates $P < 0.05$

ADSCs-EVs may alleviate uranium-induced kidney cell damage by inhibiting the TLR4/NF-κB signaling pathway

Previous studies have suggested that ADSCs-EVs can suppress the expression of TLR4 [48]. The extracellular release of mtDNA is associated with the upregulation of TLR4 expression [49]. Through the Genecards database search and utilizing the STRING database, we identified proteins interacting with TLR4 (Fig. 5A). Based on the PPI network analysis, our results indicate that TLR4 is a central gene in this network (Fig. 5B). Further enrichment analysis of GO and KEGG pathways on proteins within the PPI network revealed that these proteins are mainly enriched in immune regulation functions and the NF-kappa B signaling pathway (Fig. 5C-D). Therefore, it is speculated that ADSCs-EVs may block mtDNA-induced pyroptosis by inhibiting the TLR4/NF-κB signaling pathway.

To validate whether ADSCs-EVs mitigate uranium-induced kidney cell damage through modulating the TLR4/NF-κB signaling pathway, we treated HK-2 cells in different groups. The nuclear translocation of the p65 protein is an indicator of TLR4/NF-κB signaling pathway activation. Western blot results demonstrated (Fig. 6A-B) that compared to the Control group, the expression of TLR4 significantly increased in UA-treated HK-2 cells, along with a notable increase in nuclear p-p65 expression. Upon the addition of ADSCs-EVs, these effects were reversed. Additionally, immunofluorescence staining to detect nuclear translocation of p65 revealed (Fig. 6C) that in UA-treated HK-2 cells, p65 protein notably translocated to the nucleus, and this effect was reversed upon the addition of ADSCs-EVs. These findings indicate that UA treatment activates the TLR4/NF-κB signaling pathway to promote p65 nuclear translocation, whereas ADSCs-EVs can reverse the effects induced by UA.

Finally, when cells were treated with the NF-κB signaling pathway activator PMA, it was observed that the inhibitory effect of ADSCs-EVs on p65 nuclear translocation could be reversed (Fig. 6D-E). Further experimental observations on the functional changes in various groups of kidney cells revealed that post-PMA treatment, there was a significant upregulation in the expression of IL-1β,

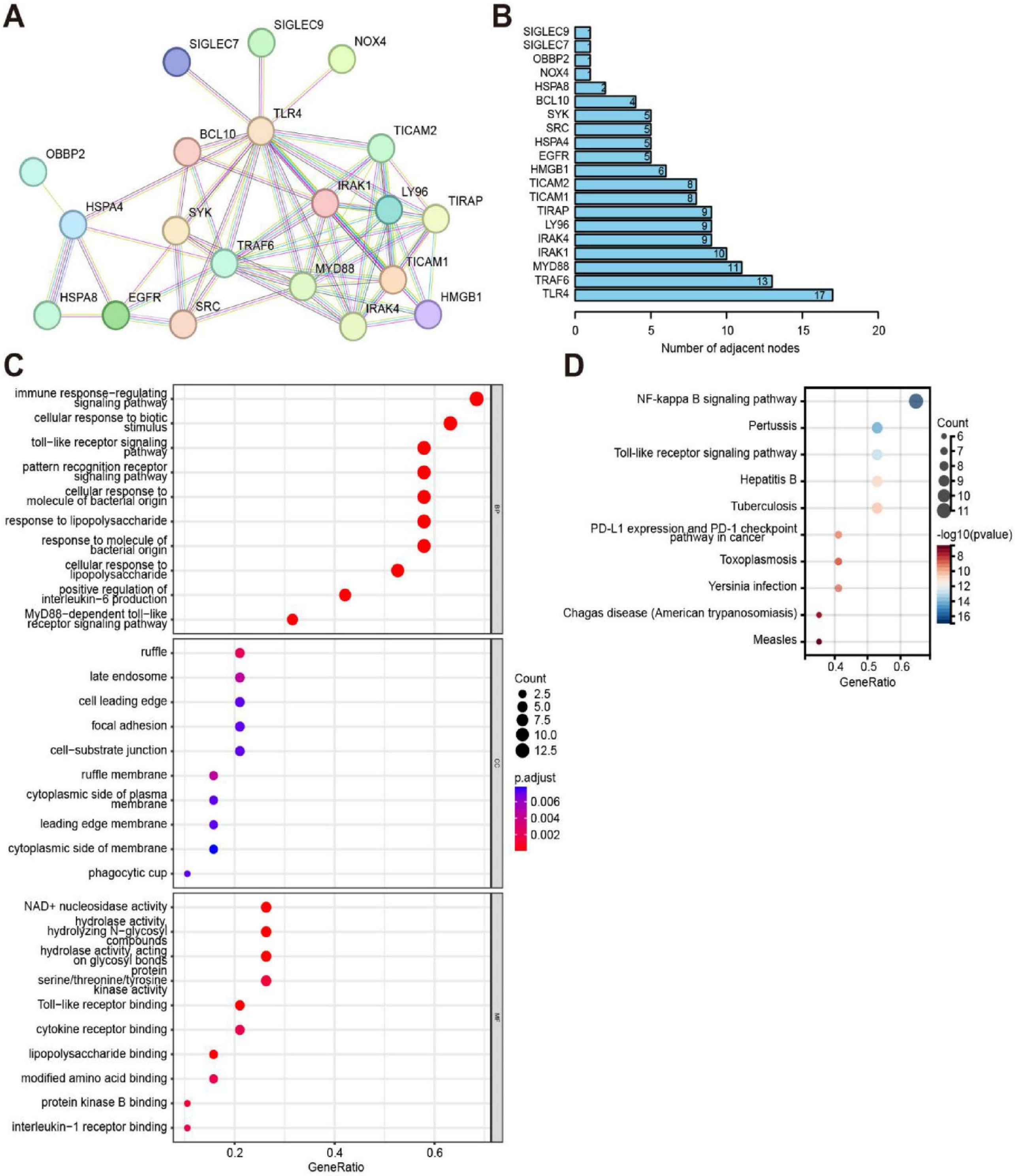

Fig. 5 Possible mechanism of ADSCs-EVs inhibition of mtDNA-mediated cell apoptosis. (**A**) PPI network constructed by obtaining proteins interacting with TLR4 from the STRING database; (**B**) Sorting of the number of adjacent nodes in the PPI network representing protein interactions; (**C**) Functional enrichment analysis of proteins in the PPI network using GO; (**D**) Enrichment analysis of KEGG pathways for proteins in the PPI network

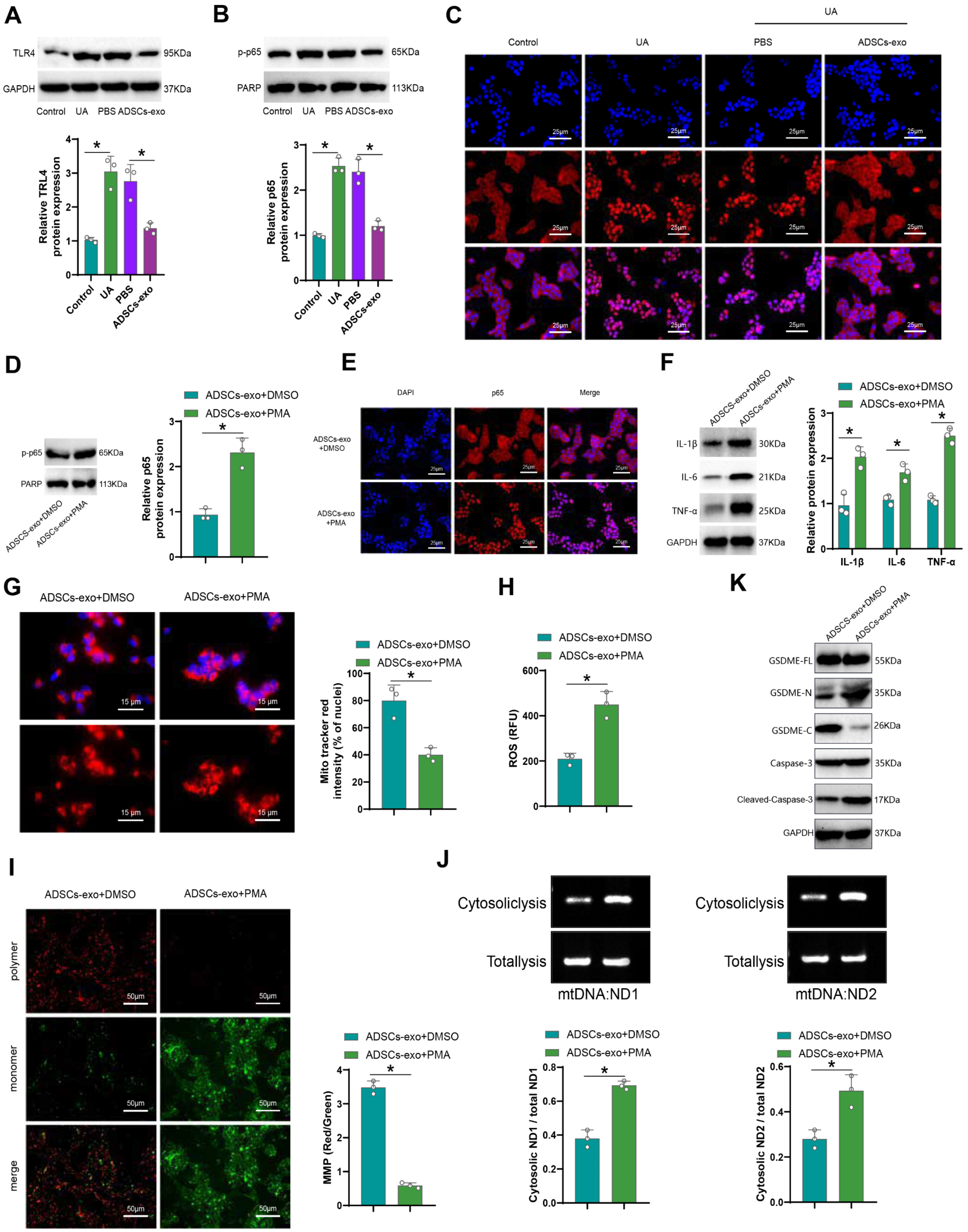

Fig. 6 (See legend on next page.)

(See figure on previous page.)

Fig. 6 Effect of ADSCs-EVs on uranium-induced renal cell injury via modulation of TLR4/NF-κB signaling pathway figure X. Overview of experimental procedures. (**A**) Western blot to assess TLR4 expression levels in various cell groups; (**B**) Western blot to detect nuclear expression of p-p65 in different cell groups; (**C**) Immunofluorescence analysis to examine nuclear translocation of p65 in various cell groups; (**D**) Western blot after PMA treatment to measure nuclear expression of p-p65 in different cell groups; (**E**) Immunofluorescence analysis post-PMA treatment to evaluate nuclear translocation of p65 in different cell groups; (**F**) Western blot for IL-1β, IL-6, and TNF-α expression in various cell groups; (**G**) Mitotracker staining to assess mitochondrial morphology in different cell groups (red, mitochondria; blue, nucleus; scale bar = 15 μm); (**H**) DCFH-DA assay to measure total ROS content in various cell groups; (**I**) JC-1 staining to evaluate MMP in different cell groups, scale bar = 50 μm; (**J**) RT-qPCR to determine cytoplasmic mtDNA copy number in various cell groups; (**K**) Western blot for activated GSDME and Caspase-3 expression in different cell groups. All cell experiments were performed in triplicate, with * indicating $P < 0.05$

IL-6, and TNF-α within the cells (Fig. 6F). Additionally, mitochondrial fragmentation in the cells was exacerbated (Fig. 6G), accompanied by a significant increase in ROS levels (Fig. 6H) and a marked reduction in the MMP, as indicated by an enhancement in the green fluorescence within the cells (Fig. 6I). These findings suggest that post-PMA treatment could reverse the reparative effect of ADSCs-EVs on mitochondrial damage in kidney cells. Moreover, following PMA treatment, there was an increase in the abundance of ND1 and ND2 (mtDNA gene segments) in the cytoplasmic fraction, while the total cellular DNA abundance remained unchanged (Fig. 6J), indicating a reversal of the blockade on mtDNA leakage by ADSCs-EVs post-PMA treatment. Furthermore, Western blot analysis of kidney pyroptosis-related proteins showed a significant increase in the expression of activated GSDME and Caspase-3 within the cells post-PMA treatment (Fig. 6K), implying that PMA treatment could reverse the inhibitory effect of ADSCs-EVs on kidney pyroptosis. In conclusion, inhibiting the TLR4/NF-κB signaling pathway can reverse the reparative effect of ADSCs-EVs on uranium-induced kidney cell damage.

Enhancement of the stability of RGD hydrogel-loaded ADSCs-EVs in vivo

In vitro cellular experiments have demonstrated the potential of ADSCs-EVs to alleviate uranium-induced renal cell injury. In the upcoming investigation, we aim to further explore the therapeutic effects of ADSCs-EVs on renal damage in vivo. However, it is known that direct injection of EVs into animal bodies may lead to rapid degradation or clearance, thereby diminishing their stability and shortening their half-life in the bloodstream. Previous studies have reported that RGD hydrogel, as a carrier, can enhance the therapeutic efficacy of EVs in heart diseases [50]. Therefore, we hypothesize that the therapeutic effects of ADSCs-EVs on renal damage could be enhanced through RGD hydrogel.

Initially, by covalently linking biotin to RGD, TEM images revealed intertwined nano-fibers formed by RGD-biotin molecules (Fig. 7A). Subsequently, when adding ADSCs-EVs to RGD hydrogel (Fig. 7B), rheological results indicated that the mechanical properties of the hydrogel do not significantly weaken when the mass ratio of ADSCs-EVs to RGD hydrogel is less than 1:1.5 (Fig. 7C). An optimal mass ratio of 1:1 was selected for rheological testing, showing no significant differences in the mechanical properties of RGD hydrogel before and after the addition of ADSCs-EVs (Fig. 7D). To further investigate the stability of RGD hydrogel at the site of renal damage, Cy5-labeled RGD hydrogel was employed to track the retention time of the hydrogel in the kidneys. The results illustrated in Fig. 7E indicate that RGD hydrogel can remain in the body for up to 7 days, suggesting excellent in vivo stability of RGD hydrogel.

To track ADSCs-EVs within the body, we employed Gluc-lactadherin labeling. Our findings (Fig. 7F) demonstrate that Gluc-lactadherin-labeled ADSCs-EVs can be internalized by HK-2 cells, showing a linear dependency between the concentration of EVs and the Gluc fluorescence signal. Subsequently, in a kidney injury model, injections of ADSCs-EVs and RGD hydrogel-loaded ADSCs-EVs were administered. The in vivo stability of the EVs was monitored through bioluminescence imaging, revealing (Fig. 7G) that the use of ADSCs-EVs/RGD hydrogel resulted in a more stable and prolonged retention compared to only ADSCs-EVs. These findings indicate that the RGD hydrogel-loaded ADSCs-EVs can enhance the in vivo stability of the ADSCs-EVs.

Enhancement of ADSCs-EVs therapeutic efficacy on kidney injury by RGD hydrogel

Based on the findings of our study, we further investigated the therapeutic effects of ADSCs-EVs on kidney injury induced by uranium in rats, as well as the role of RGD hydrogel in this process. The experimental results indicated a significant decrease in the p65-positive rate in the cell nuclei after treatment with ADSCs-EVs (Fig. 8A-B), along with a notable improvement in the morphological features of kidney tissue (Fig. 8C). Significant reductions were observed in the biochemical indicators of kidney function (urea, creatinine) and oxidative stress markers (malondialdehyde, glutathione, superoxide dismutase, etc.) (Fig. 8D). Furthermore, following treatment with ADSCs-EVs, there was a significant increase in the mRNA expression levels of mtDNA helicase (TWNK), mitochondrial transcription factor A (TFAM), mitochondrial respiratory chain complex I (MRC I), mitochondrial respiratory chain complex IV (MRC IV), mitochondrial biogenesis-related factors PGC-1α, NRF1, and NRF2

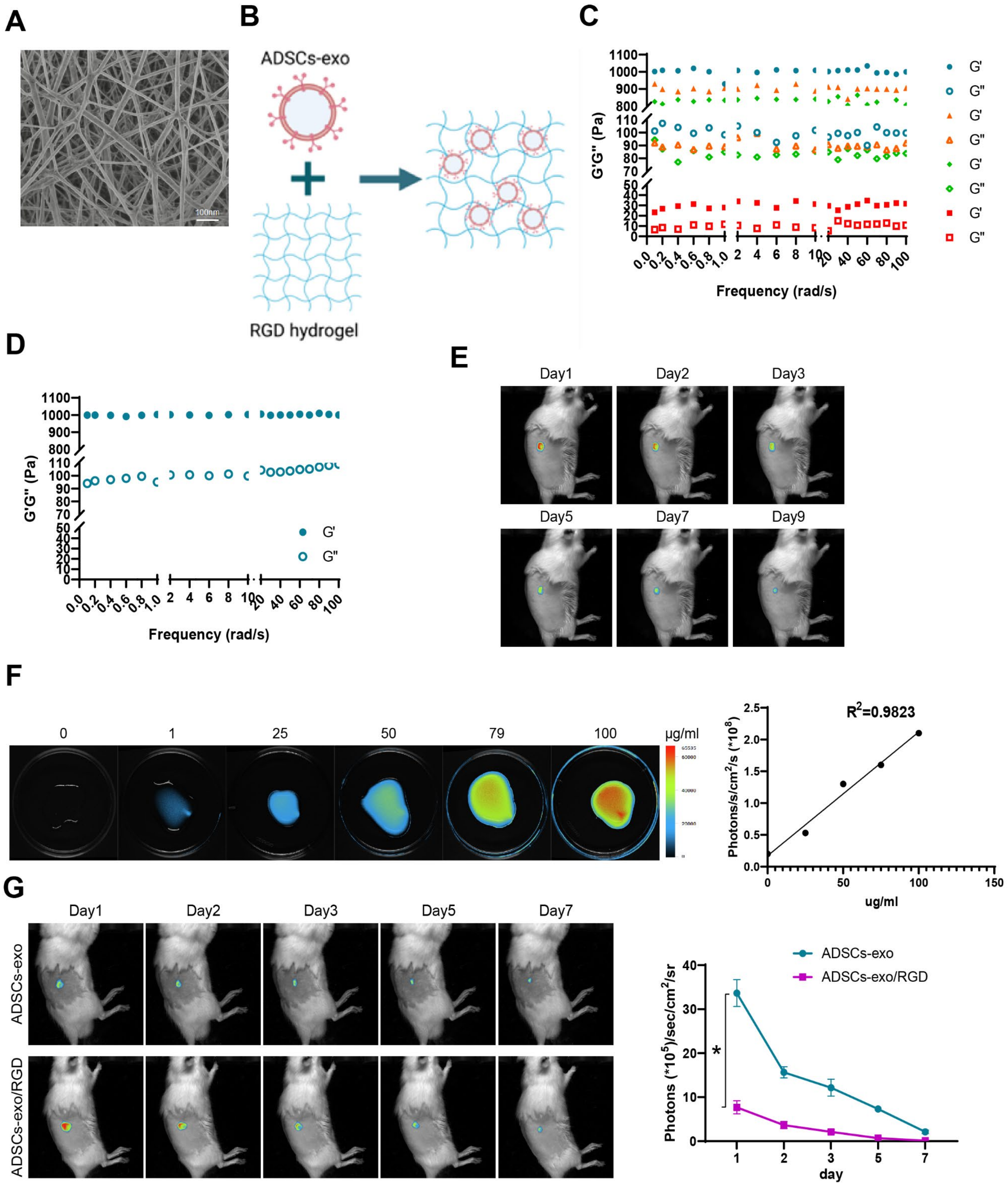

Fig. 7 Effect of RGD hydrogel-loaded ADSCs-EVs on the in vivo stability of ADSCs-EVs. (**A**) TEM image shows intertwined nanofibers; (**B**) Schematic illustration of RGD hydrogel-loaded ADSCs-EVs; (**C**) Dynamic frequency scans of ADSCs-EVs/RGD hydrogel encapsulating ADSCs-EVs at different mass ratios (0.5:1 (green), 1:1 (blue), 1.5:1 (pink), 2:1 (yellow)), where G′ represents storage modulus and G″ represents loss modulus; (**D**) Dynamic frequency scans of RGD hydrogel encapsulating ADSCs-EVs at a 1:1 mass ratio before (black) and after (blue) encapsulation, showing G′ and G″ values; (**E**) In vivo retention time of Cy5-labeled RGD hydrogel; (**F**) Bioluminescence imaging of Gluc-labeled ADSCs-EVs indicating a linear dependency between ADSCs-EVs concentration and Gluc signal; (**G**) Bioluminescence imaging tracking the in vivo stability of ADSCs-EVs. * indicates $P < 0.05$

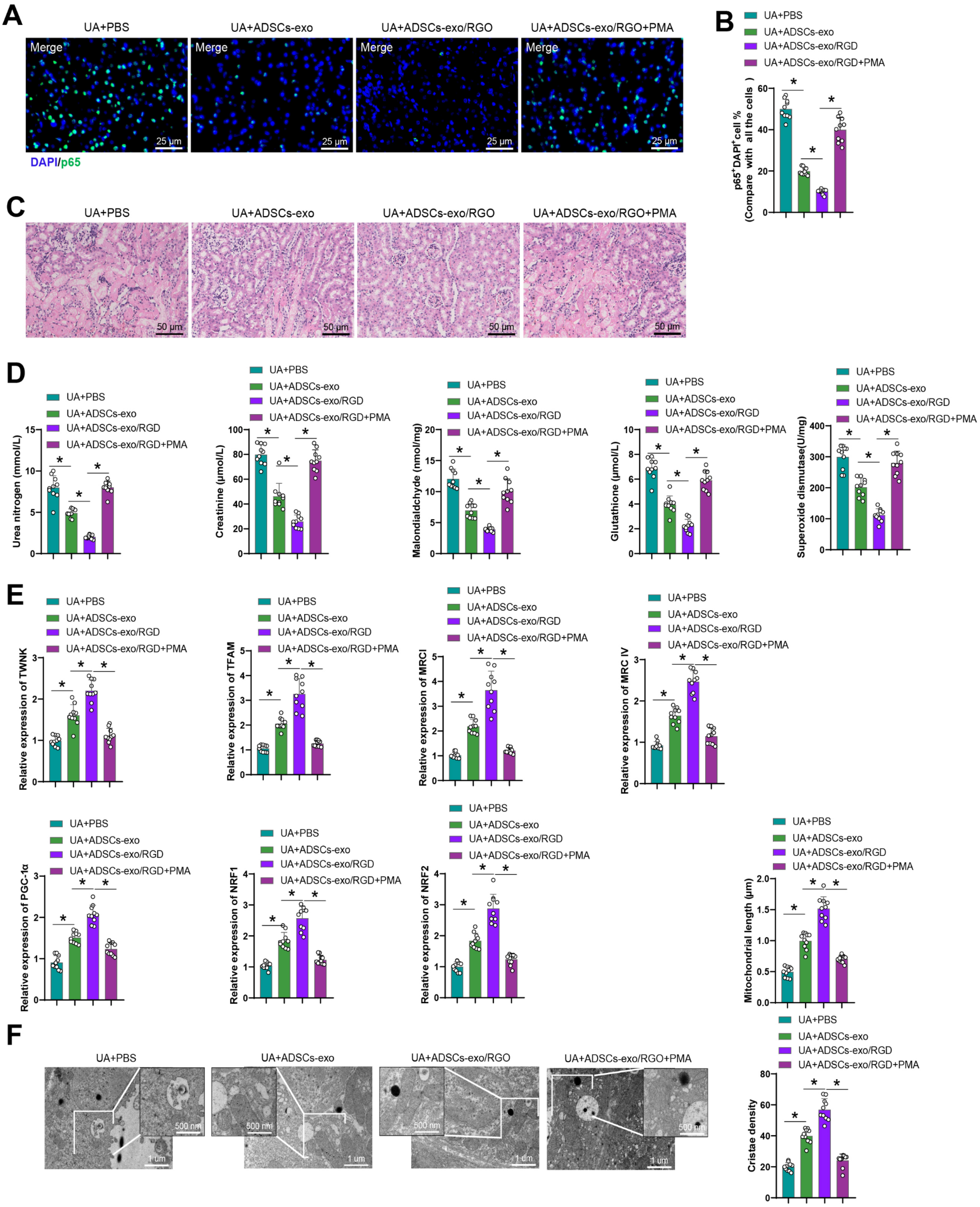

Fig. 8 Therapeutic Effects of RGD Hydrogel-Loaded ADSCs-EVs on Kidney Injury. (**A**-**B**) Immunofluorescence staining showing the colocalization of p65 with the cell nucleus in rat renal tissues of each group; (**C**) H&E staining examining the morphological structure of rat kidney tissues in each group (scale bar = 50 µm); (**D**) Assessment of urea, creatinine, malondialdehyde, glutathione, and superoxide dismutase levels in rat kidney tissues of each group; (**E**) RT-qPCR analysis of mRNA levels of relevant cytokines TWNK, TFAM, MRC I, MRC IV, PGC-1α, NRF1, and NRF2 in rat kidney tissues of each group; (**F**) TEM images displaying mitochondria in kidney tissues in each group, along with quantitative data on mitochondrial length and cristae density, Scale bars = 1 µm / 500 nm. Each group consisted of 10 rats, with * indicating $P < 0.05$

in rats (Fig. 8E). Mitochondrial fragmentation and cristae vacuolization in rat kidney tissues were significantly reduced (Fig. 8F) after treatment with ADSCs-EVs. Compared to treatment with ADSCs-EVs alone, RGD hydrogel notably enhanced the therapeutic effects of ADSCs-EVs. Additionally, the activation of the NF-κB signaling pathway by the stimulant PMA reversed the therapeutic effects of ADSCs-EVs.

Discussion

In comparison with prior studies, this research differs in terms of the studied subjects, methodologies, and outcomes. Firstly, in the choice of subjects, previous studies often focused on animal or cell models for experimentation, whereas this study employed a model of uranium-induced kidney injury. This model selection aligns more closely with real-world kidney damage scenarios, thereby offering more intuitive and reliable results [51–53].

Secondly, regarding research methodologies, prior studies predominantly concentrated on observing static indicators such as cell viability and inflammation levels, while this study emphasized the analysis of molecular mechanisms. Specifically, it investigated the inhibition of the TLR4/NF-κB signaling pathway to regulate mtDNA-mediated pyroptosis. Through this approach, the research delved deeper into understanding the specific pathways involved in ADSCs-EVs therapy for kidney injury.

Finally, concerning the outcomes, this study identified a significant alleviating effect of ADSCs-EVs on kidney injury, a conclusion that prior research may not have definitively provided. Furthermore, this study elucidated the potential mechanisms of ADSCs-EVs through further exploration, explaining its therapeutic effect, which sets it apart from previous research.

This study expands upon previous research findings and offers new insights into the field. While past studies may have suggested that ADSCs have therapeutic potential for kidney injury, our research, focusing on ADSCs-EVs, revealed a more pronounced alleviation of renal damage. This discovery holds significant clinical implications, paving the way for the development of more effective treatment strategies.

As a receptor for recognizing pathogens, TLR4 activates the NF-κB signaling pathway through the MyD88-dependent pathway, inducing the secretion of various pro-inflammatory factors such as TNF-α, IL-1β, and IL-6. These factors further exacerbate inflammation in renal tubules and the renal interstitium. Numerous in vivo and in vitro studies have demonstrated that inhibiting the TLR4/NF-κB signaling pathway can alleviate or even treat various renal injuries [54, 55]. In previous studies involving LPS-stimulated BV-2 microglial cells, ADSC-EVs significantly reduced the expression of key proteins, including TLR4, p-NFκB, and p-p38 MAPK, and decreased the production of pro-inflammatory cytokines, indicating the ability of ADSC-EVs to inhibit the TLR4/NF-κB pathway in vitro [56]. Similarly, in a mouse model of depression, ADSCs reduced the expression of CMS-induced pro-inflammatory cytokines by inhibiting the TLR4/NF-κB signaling pathway [57]. In uranium-induced renal injury, the TLR4/NF-κB signaling pathway plays a critical role in renal toxicity by regulating inflammatory responses [58, 59]. Uranium exposure upregulates the expression of inflammatory genes, such as TNF-α, iNOS, and COX-2, through activation of the NF-κB signaling pathway. The accumulation of these inflammatory factors in renal tissues further leads to oxidative stress, apoptosis, and tissue damage, ultimately resulting in acute or chronic renal dysfunction [60]. our study indicates that the molecular mechanism through which ADSCs-EVs act on kidney injury is by suppressing the TLR4/NF-κB signaling pathway to regulate mtDNA-mediated pyroptosis.

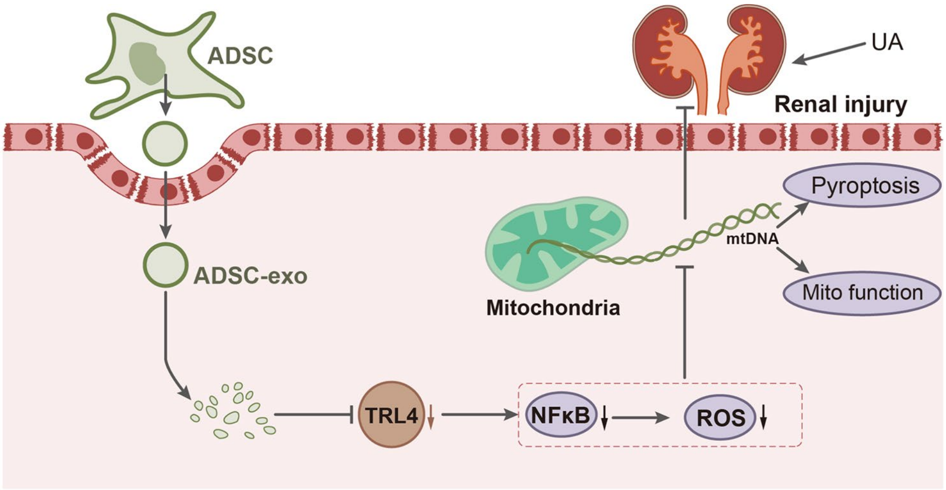

Fig. 9 ADSCs-EVs alleviate uranium-induced kidney injury by inhibiting the TLR4/NF-κB signaling pathway

This elucidation of the mechanism further explains the therapeutic effects of ADSCs-EVs and provides theoretical support for their application in treating renal damage. Additionally, we propose other potential mechanisms for future research directions.

Comparatively, our results demonstrate that ADSCs-EVs hold advantages and potential in alleviating uranium-induced renal damage. Compared to traditional drug therapies, ADSCs-EVs may offer more direct and effective treatment outcomes, reducing the direct toxicity of drugs on the kidneys [20, 61]. Furthermore, in contrast to other treatment methods, ADSCs-EVs may be more feasible and reliable as they are EVs from autologous stem cells, avoiding many issues associated with allogeneic transplants [62, 63].

The scientific significance of this study lies in gaining a profound understanding of the mechanisms underlying kidney injury and proposing a novel therapeutic strategy through ADSCs-EVs. This approach holds significant clinical potential and could present a breakthrough in the treatment of kidney diseases. Moreover, the study's implications for clinical applications are noteworthy as they can provide a foundation and guidance for therapeutic interventions.

However, the study has certain limitations. Primarily, it utilized an animal model, which may not entirely reflect human conditions. Additionally, the sample size was relatively small, requiring larger-scale clinical studies to validate the results' reliability. Furthermore, there may be inherent randomness and biases in the experimental design that need addressing.

Looking ahead, this study can further explore the detailed mechanisms of ADSCs-EVs in kidney injury. Increasing evidence suggests that EVs play a critical role in intercellular communication by transferring cytosolic proteins, RNA, lipids, and other active cargo molecules [64, 65]. Future research could utilize proteomics or RNA sequencing technologies to analyze the active substances enriched in ADSCs-EVs. Combining bioinformatics analysis with experimental validation could further elucidate the mechanisms by which ADSCs-EVs exert their effects in kidney injury, such as investigating the regulatory role of the TLR4/NF-κB signaling pathway in mtDNA-mediated pyroptosis. Additionally, further studies could examine the clinical prospects of ADSCs-EVs, including their potential applications in treating other kidney diseases and related conditions. More research is needed to delve into and validate these potential mechanisms and applications.

In conclusion, this study expands the knowledge in the field through comparison with previous research and analysis, offering new therapeutic strategies and theoretical foundations. While the findings hold significant scientific and clinical value, there are limitations that need addressing. Future research should focus on addressing these constraints and further exploring the mechanisms and potential of ADSCs-EVs in the treatment of kidney injuries to advance the field.

Conclusion

Based on the aforementioned results, we can preliminarily conclude that ADSCs-EVs primarily inhibit mtDNA-mediated pyroptosis by suppressing the TLR4/NF-κB signaling pathway, thereby alleviating uranium-induced renal damage (Fig. 9). This study successfully elucidated the molecular mechanism by which ADSCs-EVs regulate pyroptosis mediated by mtDNA through the TLR4/NF-κB signaling pathway, thus offering a novel perspective on understanding the pathogenesis of uranium-induced kidney injury.

Supplementary Information

The online version contains supplementary material available at https://doi.org/10.1186/s12951-025-03176-6.

Supplementary Material 1: Fig. S1. Identification of ADSCs and ADSCs-EVs Note: (A) Flow cytometry analysis of cell surface markers CD29, CD44, CD31, and HLA-DR. (B) Adipogenic, osteogenic, and chondrogenic differentiation of cells was assessed using Oil Red-O, Alizarin Red, and Alcian Blue staining (scale bar = 50 μm). (C) Morphological analysis of ADSCs-EVs *via* TEM. (D) Size distribution of ADSCs-EVs detected by NTA. (E) Western blot analysis of EVs-specific markers. (F) Immunofluorescence assessment of the uptake of ADSCs-EVs by HK-2 cells at different concentrations (25 μg/mL, 50 μg/mL, and 200 μg/mL). The negative control group consisted of cells co-incubated with PKH26 dye without the addition of ADSCs-EVs. scale bar = 15 μm. All cellular experiments were repeated three times

Supplementary Material 2

Acknowledgements

None.

Author contributions

Xi Chen and Chun-mei Dai contributed equally to experimental design, data analysis, and manuscript preparation. Bin Zhang, Wan-xin Zhang, and Zheng-hong Huang performed experiments and data collection. Jiu-yi Jiang and Shi-qi Hu provided technical support. Jia-hua Ma and Jia-fu Feng supervised the study, secured funding, and revised the manuscript. All authors approved the final version.

Funding

This research was supported by Science and Technology Department of Sichuan Province (2019YJ0701, 2021YJ0239and 2023NSFSC0670) and NHC Key Laboratory of Nuclear Technology Medical Transformation (Mianyang Central Hospital) (2021HYX005).

Data availability

All data can be provided as needed.

Declarations

Ethical approval

All animal experiments were approved by our hospital's animal ethics committee (No. 22-07-127) and conformed to ethical norms.

Competing interests

The authors declare no competing interests.

Author details

[1]School of Life Science and Engineering, Southwest University of Science and Technology, Mianyang, Sichuan 621010, China

[2]NHC Key Laboratory of Nuclear Technology Medical Transformation (MIANYANG CENTRAL HOSPITAL), Affiliated School of Medicine, Mianyang Central Hospital, University of Electronic Science and Technology of China, Mianyang, Sichuan 621000, China

[3]Department of Medical Laboratory, Affiliated Hospital of Southwest Medical University, Luzhou, Sichuan 646000, China

[4]College of Medical Technology, Chengdu University of Traditional Chinese Medicine, Chengdu, Sichuan 611137, China

Received: 8 August 2024 / Accepted: 29 January 2025

References

1. Ortega-Romero M, Jiménez-Córdova MI, Barrera-Hernández Á, et al. Relationship between urinary biomarkers of early kidney damage and exposure to inorganic toxins in a pediatric population of Apizaco, Tlaxcala, Mexico. J Nephrol. 2023;36(5):1383–93. https://doi.org/10.1007/s40620-023-01598-9.
2. Al-Full ZZ, Khattab MR. Uranium isotopic ratio of black shale and its role in detection of oxic-anoxic conditions of uranium depositions. J Environ Sci Health Tox Hazard Subst Environ Eng. 2022;57(5):376–85. https://doi.org/10.1080/10934529.2022.2068886.
3. Xue XM, Wu XY, Zhan JM. Zhonghua Lao Dong Wei Sheng Zhi Ye Bing Za Zhi. 2023;41(11):864–9. https://doi.org/10.3760/cma.j.cn121094-20221209-00589
4. Zhong D, Wang R, Zhang H, Wang M, Zhang X, Chen H. Induction of lysosomal exocytosis and biogenesis via TRPML1 activation for the treatment of uranium-induced nephrotoxicity. Nat Commun. 2023;14(1):3997. Published 2023 Jul 6. https://doi.org/10.1038/s41467-023-39716-7
5. Su SH, Su SJ, Huang LY, Chiang YC. Leukemic cells resist lysosomal inhibition through the mitochondria-dependent reduction of intracellular pH and oxidants. Free Radic Biol Med. 2023;198:1–11. https://doi.org/10.1016/j.freeradbiomed.2023.01.025.
6. Oduro PK, Zheng X, Wei J, et al. The cGAS-STING signaling in cardiovascular and metabolic diseases: future novel target option for pharmacotherapy. Acta Pharm Sin B. 2022;12(1):50–75. https://doi.org/10.1016/j.apsb.2021.05.011.
7. Tang C, Livingston MJ, Safirstein R, Dong Z. Cisplatin nephrotoxicity: new insights and therapeutic implications. Nat Rev Nephrol. 2023;19(1):53–72. https://doi.org/10.1038/s41581-022-00631-7.
8. Foerster EG, Mukherjee T, Cabral-Fernandes L, Rocha JDB, Girardin SE, Philpott DJ. How autophagy controls the intestinal epithelial barrier. Autophagy. 2022;18(1):86–103. https://doi.org/10.1080/15548627.2021.1909406.
9. Klionsky DJ, Abdel-Aziz AK, Abdelfatah S et al. Guidelines for the use and interpretation of assays for monitoring autophagy (4th edition)[1]. Autophagy. 2021;17(1):1-382. https://doi.org/10.1080/15548627.2020.1797280
10. Jin L, Yu B, Armando I, Han F, Mitochondrial. DNA-Mediated inflammation in Acute kidney Injury and chronic kidney disease. Oxid Med Cell Longev. 2021;2021:9985603. https://doi.org/10.1155/2021/9985603. Published 2021 Jun 29.
11. Hou J, Tolbert E, Birkenbach M, Ghonem NS. Treprostinil alleviates hepatic mitochondrial injury during rat renal ischemia-reperfusion injury. Biomed Pharmacother. 2021;143:112172. https://doi.org/10.1016/j.biopha.2021.112172.
12. Oka T, Hikoso S, Yamaguchi O et al. Mitochondrial DNA that escapes from autophagy causes inflammation and heart failure [published correction appears in Nature. 2012;490(7419):292]. Nature. 2012;485(7397):251–255. https://doi.org/10.1038/nature10992
13. West AP, Shadel GS. Mitochondrial DNA in innate immune responses and inflammatory pathology. Nat Rev Immunol. 2017;17(6):363–75. https://doi.org/10.1038/nri.2017.21.
14. Zeng X, Zhang YD, Ma RY, et al. Activated Drp1 regulates p62-mediated autophagic flux and aggravates inflammation in cerebral ischemia-reperfusion via the ROS-RIP1/RIP3-exosome axis. Mil Med Res. 2022;9(1):25. https://doi.org/10.1186/s40779-022-00383-2. Published 2022 May 27.
15. Victorelli S, Salmonowicz H, Chapman J et al. Apoptotic stress causes mtDNA release during senescence and drives the SASP [published correction appears in Nature. 2024;625(7995):E15. https://doi.org/10.1038/s41586-023-07002-7]. Nature. 2023;622(7983):627–636. https://doi.org/10.1038/s41586-023-06621-4
16. Pillalamarri N, Abdullah, Ren G, et al. Exploring the utility of extracellular vesicles in ameliorating viral infection-associated inflammation, cytokine storm and tissue damage. Transl Oncol. 2021;14(7):101095. https://doi.org/10.1016/j.tranon.2021.101095.
17. Lee M, Ban JJ, Yang S, Im W, Kim M. The exosome of adipose-derived stem cells reduces β-amyloid pathology and apoptosis of neuronal cells derived from the transgenic mouse model of Alzheimer's disease. Brain Res. 2018;1691:87–93. https://doi.org/10.1016/j.brainres.2018.03.034.
18. Li Y, Zhang J, Shi J et al. Exosomes derived from human adipose mesenchymal stem cells attenuate hypertrophic scar fibrosis by miR-192-5p/IL-17RA/Smad axis [published correction appears in Stem Cell Res Ther. 2021;12(1):490. https://doi.org/10.1186/s13287-021-02568-3]. Stem Cell Res Ther. 2021;12(1):221. Published 2021 Mar 31. https://doi.org/10.1186/s13287-021-02290-0
19. Hu J, Jiang Y, Wu X, et al. Exosomal mir-17-5p from adipose-derived mesenchymal stem cells inhibits abdominal aortic aneurysm by suppressing TXNIP-NLRP3 inflammasome. Stem Cell Res Ther. 2022;13(1):349. https://doi.org/10.1186/s13287-022-03037-1. Published 2022 Jul 26.
20. Wang Y, Niu H, Li L et al. Anti-CHAC1 exosomes for nose-to-brain delivery of miR-760-3p in cerebral ischemia/reperfusion injury mice inhibiting neuron ferroptosis. J Nanobiotechnology. 2023;21(1):109. Published 2023 Mar 27. https://doi.org/10.1186/s12951-023-01862-x
21. Kim YS, Aum J, Kim BH, et al. Therapeutic effect of three-Dimensional cultured adipose-derived stem cell-conditioned medium in Renal Ischemia-Reperfusion Injury. Int J Stem Cells. 2023;16(2):168–79. https://doi.org/10.15283/ijsc22137.
22. Bian Z, Wang X, Zhu R, Chen S. Mir-21-5p in extracellular vesicles obtained from adipose tissue-derived stromal cells facilitates tubular epithelial cell repair in acute kidney injury. Cytotherapy. 2023;25(3):310–22. https://doi.org/10.1016/j.jcyt.2022.08.002.
23. Zhu M, Ye M, Wang J, Ye L, Jin M. Construction of Potential miRNA-mRNA Regulatory Network in COPD plasma by Bioinformatics Analysis. Int J Chron Obstruct Pulmon Dis. 2020;15:2135–45. https://doi.org/10.2147/COPD.S255262. Published 2020 Sep 10.
24. Pan H, Guo C, Pan J, et al. Construction of a competitive endogenous RNA network and identification of potential Regulatory Axis in Gastric Cancer. Front Oncol. 2019;9:912. https://doi.org/10.3389/fonc.2019.00912. Published 2019 Oct 4.
25. Hao Y, Huang J, Gu Y, et al. Metallothionein deficiency aggravates depleted uranium-induced nephrotoxicity. Toxicol Appl Pharmacol. 2015;287(3):306–15. https://doi.org/10.1016/j.taap.2015.06.019.
26. Qian X, Yang L. ROCK2 knockdown alleviates LPS-induced inflammatory injury and apoptosis of renal tubular epithelial cells via the NF-κB/NLRP3 signaling pathway. Exp Ther Med. 2022;24(3):603. https://doi.org/10.3892/etm.2022.11540. Published 2022 Jul 28.
27. Oh BM, Lee SJ, Park GL, et al. Erastin inhibits septic shock and inflammatory gene expression via suppression of the NF-κB pathway. J Clin Med. 2019;8(12):2210. https://doi.org/10.3390/jcm8122210. Published 2019 Dec 14.
28. Lu P, Zheng H, Meng H et al. Mitochondrial DNA induces nucleus pulposus cell pyroptosis via the TLR9-NF-κB-NLRP3 axis. J Transl Med. 2023;21(1):389. Published 2023 Jun 15. https://doi.org/10.1186/s12967-023-04266-5
29. Yu Z, Xiao Z, Guan L, et al. Translocation of gasdermin D induced mitochondrial injury and mitophagy mediated quality control in lipopolysaccharide related cardiomyocyte injury. Clin Transl Med. 2022;12(8):e1002. https://doi.org/10.1002/ctm2.1002.
30. te Poele JA, van Kleef EM, van der Wal AF, Dewit LG, Stewart FA. Radiation-induced glomerular thrombus formation and nephropathy are not prevented by the ADP receptor antagonist clopidogrel. Int J Radiat Oncol Biol Phys. 2001;50(5):1332–8. https://doi.org/10.1016/s0360-3016(01)01617-0.
31. Chen R, Xu H, Guo Z, Zhang P, Chen J, Chen Z. CID16020046, a GPR55 antagonist, attenuates sepsis–induced acute kidney injury. Mol Med Rep. 2022;25(5):155. https://doi.org/10.3892/mmr.2022.12671.
32. Fang Y, Tian Y, Huang Q et al. Deficiency of TREK-1 potassium channel exacerbates blood-brain barrier damage and neuroinflammation after intracerebral hemorrhage in mice. J Neuroinflammation. 2019;16(1):96. Published 2019 May 9. https://doi.org/10.1186/s12974-019-1485-5
33. Bao Y, Wang D, Li Z, et al. Efficacy of a novel chelator BPCBG for removing uranium and protecting against uranium-induced renal cell damage in rats

and HK-2 cells. Toxicol Appl Pharmacol. 2013;269(1):17–24. https://doi.org/10.1016/j.taap.2013.02.010.

34. Yuan Y, Zheng J, Zhao T, Tang X, Hu N. Uranium-induced rat kidney cell cytotoxicity is mediated by decreased endogenous hydrogen sulfide (H^2S) generation involved in reduced Nrf2 levels. Toxicol Res (Camb). 2016;5(2):660–73. https://doi.org/10.1039/c5tx00432b. Published 2016 Jan 27.
35. Belghali S, Ben Abderrahim K, Mahmoud I, et al. Brief Michigan Hand Outcomes Questionnaire in rheumatoid arthritis: a cross-sectional study of 100 patients. Hand Surg Rehabil. 2017;36(1):24–9. https://doi.org/10.1016/j.hansur.2016.09.003.
36. Mushahary D, Spittler A, Kasper C, Weber V, Charwat V. Isolation, cultivation, and characterization of human mesenchymal stem cells. Cytometry A. 2018;93(1):19–31. https://doi.org/10.1002/cyto.a.23242.
37. Figueroa-Valdés AI, de la Fuente C, Hidalgo Y, et al. A chemically defined, Xeno- and blood-free culture medium sustains increased production of small extracellular vesicles from mesenchymal stem cells. Front Bioeng Biotechnol. 2021;9:619930. https://doi.org/10.3389/fbioe.2021.619930. Published 2021 May 26.
38. Huang LH, Rau CS, Wu SC, et al. Identification and characterization of hADSC-derived exosome proteins from different isolation methods. J Cell Mol Med. 2021;25(15):7436–50. https://doi.org/10.1111/jcmm.16775.
39. Zhang C, Shang Y, Chen X, et al. Supramolecular nanofibers containing arginine-Glycine-aspartate (RGD) peptides boost therapeutic efficacy of Extracellular vesicles in kidney repair. ACS Nano. 2020;14(9):12133–47. https://doi.org/10.1021/acsnano.0c05681.
40. Zhou J, Li X, Wu X, et al. Exosomes released from Tumor-Associated macrophages transfer miRNAs that induce a Treg/Th17 Cell Imbalance in Epithelial Ovarian Cancer. Cancer Immunol Res. 2018;6(12):1578–92. https://doi.org/10.1158/2326-6066.CIR-17-0479.
41. Zhai L, Tai WL, Pan YQ, et al. Expression of EZH2 and P53 and their correlation in ovarian cancer tissues. Int J Clin Exp Pathol. 2020;13(3):456–64. Published 2020 Mar 1.
42. Duan M, Fang M, Wang C, Wang H, Li M. LncRNA EMX2OS induces Proliferation, Invasion and Sphere formation of ovarian Cancer cells via regulating the miR-654-3p/AKT3/PD-L1 Axis [retracted in: Cancer Manag Res. 2024;16:67–68. Doi: 10.2147/CMAR.S460242]. Cancer Manag Res. 2020;12:2141–54. https://doi.org/10.2147/CMAR.S229013. Published 2020 Mar 24.
43. Cao JY, Wang B, Tang TT et al. Exosomal miR-125b-5p deriving from mesenchymal stem cells promotes tubular repair by suppression of p53 in ischemic acute kidney injury [published correction appears in Theranostics. 2024;14(8):3080. https://doi.org/10.7150/thno.79609]. Theranostics. 2021;11(11):5248–5266. Published 2021 Mar 11. https://doi.org/10.7150/thno.54550.
44. Soranno DE, Rodell CB. Novel therapeutics: can Hydrogels work to treat kidney disease? Nephron. 2023;147(12):769–73. https://doi.org/10.1159/000531917.
45. Marchi S, Guilbaud E, Tait SWG, Yamazaki T, Galluzzi L. Mitochondrial control of inflammation. Nat Rev Immunol. 2023;23(3):159–73. https://doi.org/10.1038/s41577-022-00760-x.
46. Li N, Wang Y, Wang X, Sun N, Gong YH. Pathway network of pyroptosis and its potential inhibitors in acute kidney injury. Pharmacol Res. 2022;175:106033. https://doi.org/10.1016/j.phrs.2021.106033.
47. Li X, Liao J, Su X, et al. Human urine-derived stem cells protect against renal ischemia/reperfusion injury in a rat model via exosomal miR-146a-5p which targets IRAK1. Theranostics. 2020;10(21):9561–78. https://doi.org/10.7150/thno.42153. Published 2020 Jul 25.
48. Duan Y, Luo Q, Wang Y, et al. Adipose mesenchymal stem cell-derived extracellular vesicles containing microRNA-26a-5p target TLR4 and protect against diabetic nephropathy. J Biol Chem. 2020;295(37):12868–84. https://doi.org/10.1074/jbc.RA120.012522.
49. Wu B, Ni H, Li J, et al. The impact of circulating mitochondrial DNA on Cardiomyocyte apoptosis and myocardial Injury after TLR4 activation in experimental autoimmune myocarditis. Cell Physiol Biochem. 2017;42(2):713–28. https://doi.org/10.1159/000477889.
50. Wang Q, Zhang L, Sun Z, et al. HIF-1α overexpression in mesenchymal stem cell-derived exosome-encapsulated arginine-glycine-aspartate (RGD) hydrogels boost therapeutic efficacy of cardiac repair after myocardial infarction. Mater Today Bio. 2021;12:100171. https://doi.org/10.1016/j.mtbio.2021.100171. Published 2021 Nov 27.
51. Urowitz MB, Aranow C, Asukai Y, et al. Impact of Belimumab on Organ damage in systemic Lupus Erythematosus. Arthritis Care Res (Hoboken). 2022;74(11):1822–8. https://doi.org/10.1002/acr.24901.
52. Solanki YS, Agarwal M, Gupta AB, Gupta S, Shukla P. Fluoride occurrences, health problems, detection, and remediation methods for drinking water: a comprehensive review. Sci Total Environ. 2022;807(Pt 1):150601. https://doi.org/10.1016/j.scitotenv.2021.150601.
53. Kane-Gill SL, Meersch M, Bell M. Biomarker-guided management of acute kidney injury. Curr Opin Crit Care. 2020;26(6):556–62. https://doi.org/10.1097/MCC.0000000000000777.
54. Wang J, Chen Z, Hou S, Liu Z, Lv Q. TAK-242 attenuates crush Injury Induced Acute kidney Injury through Inhibiting TLR4/NF-κB signaling pathways in rats. Prehosp Disaster Med. 2020;35(6):619–28. https://doi.org/10.1017/S1049023X20001132.
55. Rui Y, Li S, Luan F, Li D, Liu R, Zeng N. Several alkaloids in Chinese Herbal Medicine Exert Protection in Acute kidney Injury: focus on mechanism and target analysis. Oxid Med Cell Longev. 2022;2022:2427802. https://doi.org/10.1155/2022/2427802. Published 2022 May 13.
56. Ji S, Peng Y, Liu J, Xu P, Tang S. Human adipose tissue-derived stem cell extracellular vesicles attenuate ocular hypertension-induced retinal ganglion cell damage by inhibiting microglia- TLR4/MAPK/NF-κB proinflammatory cascade signaling. Acta Neuropathol Commun. 2024;12(1):44. Published 2024 Mar 19. https://doi.org/10.1186/s40478-024-01753-8
57. Huang X, Fei GQ, Liu WJ, et al. Adipose-derived mesenchymal stem cells protect against CMS-induced depression-like behaviors in mice via regulating the Nrf2/HO-1 and TLR4/NF-κB signaling pathways. Acta Pharmacol Sin. 2020;41(5):612–9. https://doi.org/10.1038/s41401-019-0317-6.
58. Yi J, Yuan Y, Zheng J, Hu N. Hydrogen sulfide alleviates uranium-induced kidney cell apoptosis mediated by ER stress via 20S proteasome involving in Akt/GSK-3β/Fyn-Nrf2 signaling. Free Radic Res. 2018;52(9):1020–9. https://doi.org/10.1080/10715762.2018.1514603.
59. Zheng J, Zhao T, Yuan Y, Hu N, Tang X. Hydrogen sulfide (H2S) attenuates uranium-induced acute nephrotoxicity through oxidative stress and inflammatory response via Nrf2-NF-κB pathways. Chem Biol Interact. 2015;242:353–62. https://doi.org/10.1016/j.cbi.2015.10.021.
60. Guéguen Y, Frerejacques M. Review of knowledge of Uranium-Induced kidney toxicity for the development of an adverse outcome pathway to renal impairment. Int J Mol Sci. 2022;23(8):4397. https://doi.org/10.3390/ijms23084397. Published 2022 Apr 15.
61. Chang TH, Wu CS, Chiou SH, Chang CH, Liao HJ. Adipose-Derived Stem Cell Exosomes as a Novel Anti-Inflammatory Agent and the Current Therapeutic Targets for Rheumatoid Arthritis. Biomedicines. 2022;10(7):1725. Published 2022 Jul 18. https://doi.org/10.3390/biomedicines10071725
62. Wu B, Feng J, Guo J et al. ADSCs-derived exosomes ameliorate hepatic fibrosis by suppressing stellate cell activation and remodeling hepatocellular glutamine synthetase-mediated glutamine and ammonia homeostasis. Stem Cell Res Ther. 2022;13(1):494. Published 2022 Oct 4. https://doi.org/10.1186/s13287-022-03049-x
63. Shao X, Qin J, Wan C, et al. ADSC exosomes Mediate lncRNA-MIAT Alleviation of Endometrial Fibrosis by regulating miR-150-5p. Front Genet. 2021;12:679643. https://doi.org/10.3389/fgene.2021.679643. Published 2021 Jun 9.
64. Raposo G, Stoorvogel W. Extracellular vesicles: exosomes, microvesicles, and friends. J Cell Biol. 2013;200(4):373–83. https://doi.org/10.1083/jcb.201211138.
65. Seo HA, Moeng S, Sim S, Kuh HJ, Choi SY, Park JK. MicroRNA-Based Combinatorial Cancer Therapy: effects of MicroRNAs on the efficacy of Anti-cancer therapies. Cells. 2019;9(1):29. https://doi.org/10.3390/cells9010029. Published 2019 Dec 20.

Publisher's note